LOW-ANGLE NORMAL FAULTING IN THE BASIN AND RANGE-COLORADO PLATEAU TRANSITION ZONE DURING THE JANUARY 3, 2011 CIRCLEVILLE, UT EARTHQUAKE SEQUENCE

by

Christine Naomi Louise Gammans

A thesis submitted to the faculty of
The University of Utah
in partial fulfillment of the requirements for the degree of

Master of Science

in

Geophysics

Department of Geology and Geophysics

The University of Utah

August 2013

The University of Utah Graduate School

STATEMENT OF THESIS APPROVAL

The thesis of **Christine Naomi Louise Gammans**

has been approved by the following supervisory committee members:

Keith D. Koper	, Chair	**06/10/2013** Date Approved
Kristine L. Pankow	, Member	**06/10/2013** Date Approved
John M. Bartley	, Member	**06/10/2013** Date Approved

and by **D. Kip Solomon** , Chair of

the Department of **Geology and Geophysics**

and by Donna M. White, Interim Dean of The Graduate School.

ABSTRACT

On January 3, 2011, an M_w 4.5 earthquake occurred in the Tushar Mountains near Circleville, Utah (38.248°N, -112.329°W, 7.75 km depth, and origin time of 12:06:36.58). The Tushar Mountains are located in the transition zone between the stable Colorado Plateau (CP) to the east and the deforming Basin and Range (BR) province to the west. In this area, seismicity associated with the Intermountain Seismic Belt is relatively common. The University of Utah Seismograph Stations (UUSS) detected and located 97 aftershocks in the 33 weeks following the mainshock. On January 6, UUSS installed a portable station in the source region. Using three aftershocks recorded by the portable station as master events, including the largest (M_w 3.8), we relocated the mainshock/aftershock sequence. These refined locations were used as initial locations for the HypoDD method of Waldhauser and Ellsworth [2001] to produce a second, improved set of relocations. In addition to P- and S-arrival time picks, we used the lag-times from waveform cross-correlations as input to HypoDD. We analyzed the fault geometry apparent in the final locations by comparing them to known moment-tensor focal planes and by applying principal component analysis to measure the degree of planarity and orientation of the sequence as a whole. Additionally, using cross-correlation analysis, we identified aftershocks best suited for an empirical Green's function analysis of the mainshock and a strike-slip aftershock that occurred on January 6. From the events chosen by cross-correlation, we were able to obtain source-time

functions that were used to obtain fault dimensions, stress drops, and evidence for or against directivity. Lastly, we determined focal mechanisms for ten of the events using first-motion methods. The results of the combined analyses indicate that the mainshock occurred on a low-angle normal fault and that the entire sequence occurred on at least two different fault planes.

TABLE OF CONTENTS

LIST OF FIGURES

LIST OF TABLES

ACKNOWLEDGEMENTS

I would like to thank Dr. Kris Pankow and Dr. Keith Koper for serving as my primary advisors and committee members and for helping me to form and complete this project. I particularly appreciate your help working with the hypoDD relocations, the plane comparison analysis, principal component analysis, empirical Green's functions, and stress drop calculations. I enjoyed working with you both immensely and I appreciate all you have taught me over the last two years. I would also like to thank John Bartley for serving as my third committee member and working closely with me to understand the regional geology and to put this thesis into the proper context.

I would like to Jim Pechmann for constructing the initial velocity and helping me to update the model as well as working with me on the Master Event relocations and the empirical Green's function calculations. I would also like to thank Katherine Whidden for helping me with the focal mechanisms, and Mark Hale for so patiently teaching me how to pick earthquakes.

Furthermore, I owe thanks for my funding and support to the University of Utah Seismograph Stations for gifting me with the Walter J. Arabasz fellowship and guaranteeing me with two full years of support. I also would like to thank the Chevron Corporation for granting me their Geophysicist's Fellowship.

Thank you to all my fellow graduate students and office mates for making this an enjoyable two years- Glynis Jehle, Danielle D'Alfonso, Oner Sufri, Yao Yao, Kevin Kwong, Lisa Linville, Kevin Jenson, Stephanie Whittaker, and Hans Anderson.

Lastly, thank you to Brendan Sullivan for his continuous support and encouragement throughout this process. And thank you to my family, for loving and supporting and helping me to reach this point over the last 24 years of my life.

Thank You. I love you all!

CHAPTER 1

INTRODUCTION

The Intermountain Seismic Belt (ISB) is a region of seismicity that extends from northern Arizona through central Utah, along the Wyoming-Idaho border, and terminates in northwestern Montana [*Smith and Arabasz*, 1991]. In southern and central Utah, the ISB is most prominent in the transition zone (TZ) between the Basin and Range (BR) and the Colorado Plateau (CP) (Figure 1), a region which has undergone compression, extension, and magmatic activity during the Cenozoic [*Wannamaker et al.*, 2001]. The TZ is an approximately 100 km-wide region where tectonic forces transition from the stable CP to an extensional regime in the BR. The region was formerly a compressional regime, and Mesozoic-Paleocene thrust faults have been identified using subsurface exploration methods to underlie regions of the TZ, notably the Sevier Valley region to the north [*Standlee*, 1982]. These thrust structures can affect the depth distribution of seismicity [*Arabasz and Julander*, 1986], and may possibly reactivate as normal faults.

The Marysvale volcanic field is also located within the TZ (Figure 1). The Marysvale field became active at approximately 35 Ma and produced calc-alkaline lava flows, mud flows, and ash-flow tuffs. At about 20 Ma, there was a transition to still-ongoing bimodal (basalt and rhyolite) effusive volcanism [*Rowley*, 1998]. Igneous

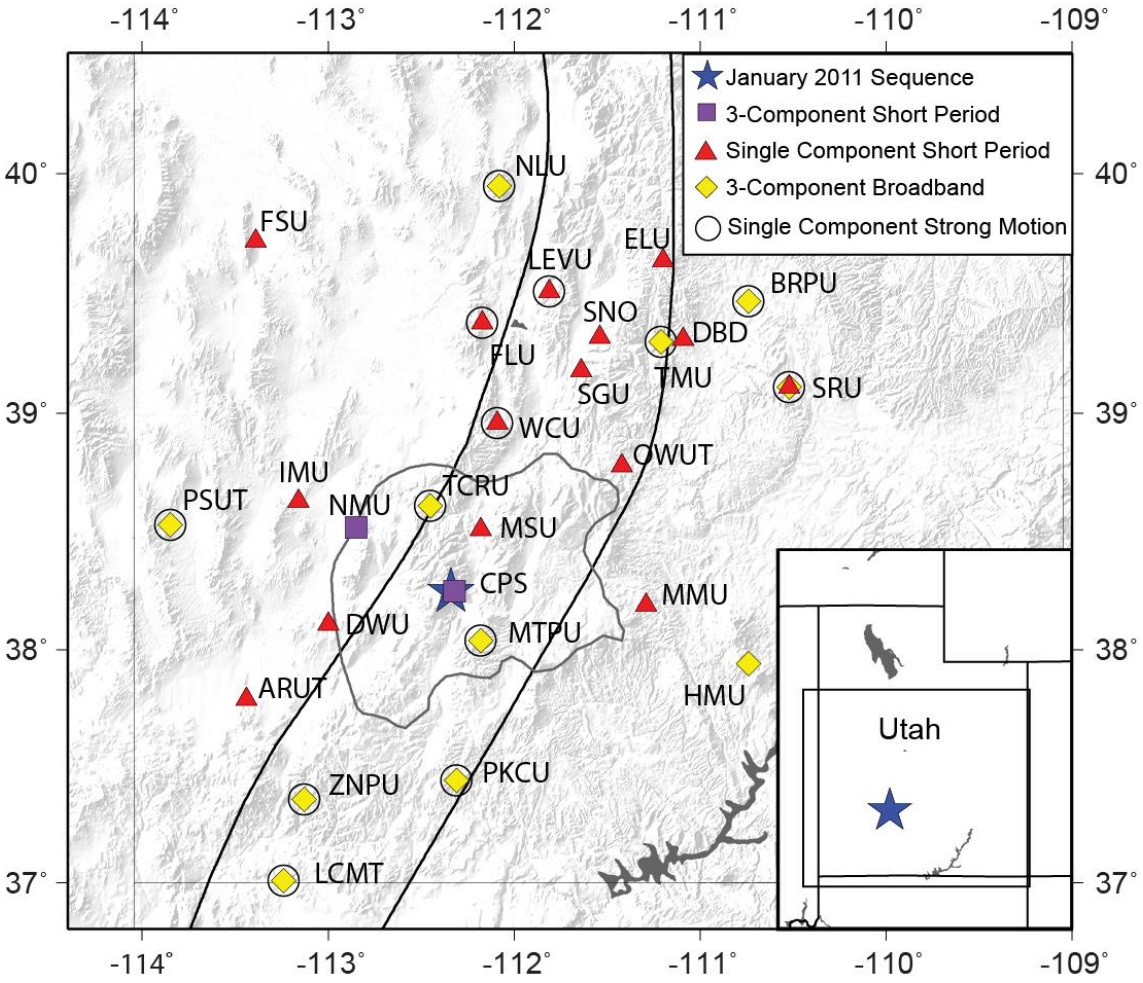

Figure 1. Map of study region (location shown by inset map). Circleville mainshock (star), UUSS seismometers (see key), and approximate boundaries for the transition zone (parallel black lines), Marysvale volcanic field (roughly circular area outlined in dark gray).

deposits from the Marysvale volcanic field are intrusive and extrusive and younger than the surrounding region, likely disrupting subsurface geology including older structures which may include thrust faults. Regardless, the effects of Marysvale magmatism on crustal structure are probably significant, but these effects are poorly understood and, therefore, it is difficult to predict their consequences for seismicity.

The University of Utah Seismograph Stations (UUSS) has been actively monitoring the ISB in Utah since 1962 and, as of 2011, has stations spread throughout the TZ (Figure 1). However, earthquake locations, particularly depth, are not always well constrained. Regional earthquakes are typically small, M_w<4.5, and depths are typically less than 15-20 km. The current network is generally too sparse to accurately constrain depths because of the need for at least one station within one focal depth of the event [*Gomberg et al.*, 1990]. Furthermore, events with M<6 do not produce surface ruptures which might reduce uncertainties in event locations. Portable networks have been deployed in previous studies to record aftershocks and obtain additional information [*Arabasz and Julander*, 1986], but deployments of multiple instruments have not been performed recently. The UUSS still deploys portable stations for large events or events of significant interest such as the 2007 Crandall Canyon mine collapse [*Pechmann et al.*, 2008].

On January 3, 2011, an M_w 4.5 earthquake occurred in southern Utah (38.248°, -112.329°, and 7.75 km depth at 12:06:36.58) outside of the city of Circleville and within the Marysvale volcanic field. Ninety-seven aftershocks were recorded in the vicinity over the course of 33 weeks, including three aftershocks of M_w > 3.2, two of which are normal and one strike-slip [*Whidden and Pankow*, 2012]. The mainshock was

located in the middle of the UUSS seismic network although the nearest station was approximately 25 km away, outside of the ideal range of one focal depth. On January 6, the UUSS deployed a portable three-component station in the epicentral region that recorded aftershocks on January 10, 12, 13, and 14. The event recorded on January 12 was the largest aftershock of the entire sequence, with M_w3.8. The portable station provided data key to constraining earthquake locations, particularly the depth, of the second largest event in the sequence and, subsequently, the absolute locations of the entire sequence.

For this study, we constructed a new velocity model for the Marysvale region. We then used the velocity model to locate and relocate the earthquakes using multiple methods. Using precise final locations, we analyzed the fault geometry by comparing the first-motion and moment-tensor focal mechanism planes to the final event locations, and by using principal component analysis. Lastly, we used an empirical Green's function deconvolution to obtain source-time functions to determine rupture times and dimensions, as well as approximate stress drops, for the mainshock and the large strike-slip aftershock. From the results, we built a picture of geophysical processes in the region, demonstrating the complexity of the region including the presence of low-angle normal faults, potentially reactivated low-angle thrust fault remnants from compression, and activation of multiple fault planes producing events of different mechanisms.

CHAPTER 2

EARTHQUAKE LOCATIONS

2.1 Velocity Model

The earthquake source region, the Marysvale volcanic field and the TZ, is geologically complicated, and ideally a 3-D velocity model would be employed to account for complexities of the subsurface structure. Unfortunately, no such model is currently available. Instead, we use 1-D velocity models for both the BR and the CP to represent the regional crustal structure.

For both BR and CP starting models, we combine two P-wave velocity models used by the UUSS for this region, the Trail Mountain model [*Arabasz et al.*, 2002] and a model developed by *Julander* [1983]. *Julander* [1983] constructed a P-wave velocity model for the upper 10 km of the crust in the Marysvale region. Julander's model, with a datum of 1500 meters, was overlain on the Trail Mountain model which extends from 10 km past 45 km. The S-velocity model is calculated assuming a Vp/Vs ratio of 1.74, a value typically used by the UUSS. The Vp/Vs ratio for the top 2.04 km of the Trail Mountain model was shown to be 1.96 using the station-pair method [*Arabasz et al*. 2002]. Therefore, S-velocities were calculated from the P-velocities using Vp/Vs=1.74, except for the topmost 1.70 km, the layer depth most comparable to the Trail Mountain model, and the elevation correction, where Vp/Vs=1.96 was used.

Initial locations were determined by manually picking P- and S-wave arrival times and using the program HYPOINVERSE [*Klein*, 1978] to obtain hypocenter locations. P-waves were picked on all available stations, but S-waves were picked on the vertical component (using the north and east components as a guide) of 3-component stations within 80 km of the event based on approximate travel time. Initial locations consistently over-predicted the S-arrival times, indicating a problem in the velocity model.

To improve the S-wave velocity model, the station-pair method was applied to observed P- and S-arrival times to calculate a new Vp/Vs ratio. Four 3-component stations were used to calculate the P- and S-wave travel-time difference: MTPU, TCRU, NMU, and CPS (the portable station installed after the main event). The station-pair method requires P- and S-phase picks at a minimum of two stations. For all events that met this requirement, the difference in P- and S-wave arrival times, P_{diff} and S_{diff}, was calculated from all available combinations of the four stations. The values of P_{diff} and S_{diff} were plotted against each other (Figure 2), and then a trendline was fit to the data using a linear least-squares regression forced through the origin, the slope of which is the Vp/Vs ratio which, in this instance, is 1.67 ± 0.02 at the 2σ confidence level.

To update the S-wave model, we again used a Vp/Vs of 1.96 for the top 1.70 km which were treated as highly heterogeneous layers from processes such as weathering and cracking. However, the Vp/Vs averaged from calculated P and S travel-times should be ~1.67. Therefore, the Vp/Vs at greater depths was lowered to 1.64 to ensure that predicted travel-times reasonably match observed travel-times.

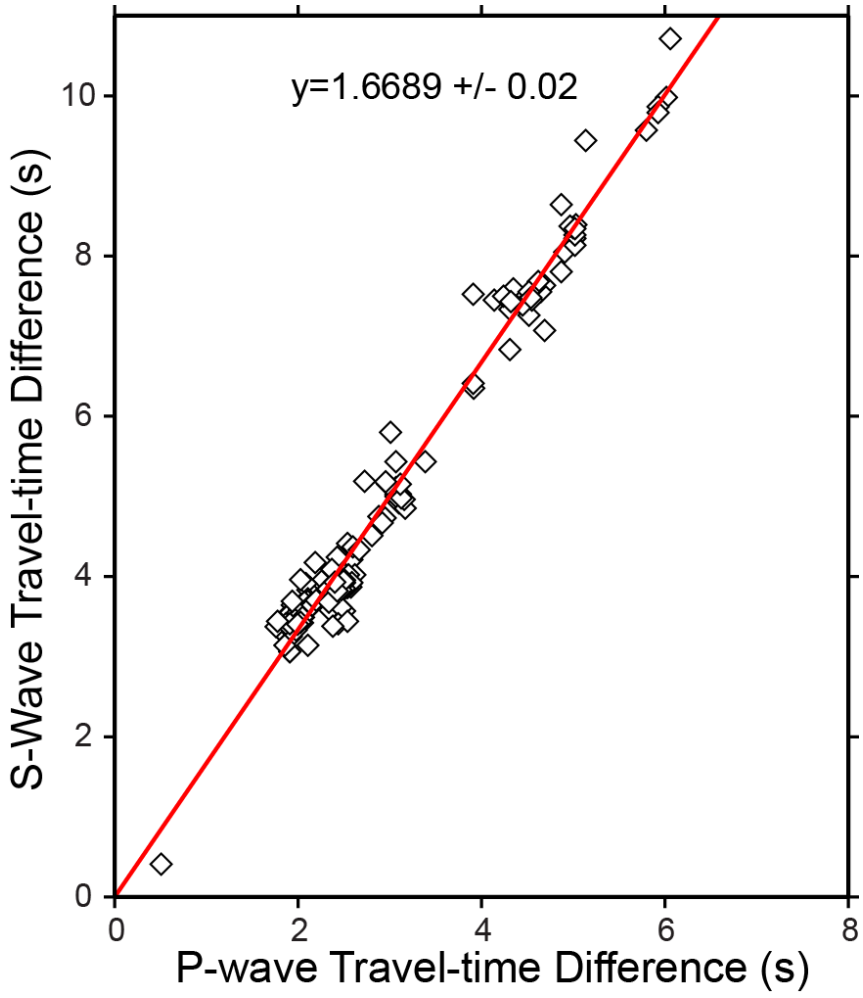

Figure 2. Station pair method results. The slope of the red trendline is the Vp/Vs ratio. The trendline fits the data with a 2σ error of 0.02 and was forced through zero as a physical constraint.

The final BR and CP velocity models are displayed in Figure 3. The upper 10 km of both models have the same layer thicknesses, but the BR model has consistently lower velocities than the CP model, as well as an additional layer below 10 km depth. Increasing the S-velocities in the models for both the BR and CP decreased the root-mean-square (RMS) errors by approximately 20% from 0.20 to 0.14 seconds. The median horizontal uncertainties decreased from 600 to 400 meters and the median uncertainties from 1600 to 1100 meters. The new velocity model significantly improved the locations, but they are still somewhat diffuse within the region (Figure 4), and the depths are not yet well enough resolved for further analyses, indicating the need for the following relocation methods.

2.2 Master Event Relocations

Using the new velocity model, we located all 98 events in the sequence using HYPOINVERSE with a cosine-tapered distance weighting from 120 km to 150 km in order to minimize the effects of far-field crustal structure on location uncertainties. Nineteen UUSS stations satisfied the 150 km minimum distance, including the portable station deployed after the mainshock (Figure 1). The portable station (CPS) installed on January 6, 2012, captured 8 aftershocks from January 10 through January 19. These events occurred within one focal depth of the portable station and therefore, unlike other events, focal depths of these events are well resolved. We used three of these well-constrained events as master events in order to improve locations and uncertainties for the remainder of events [*Corbett*, 1984].

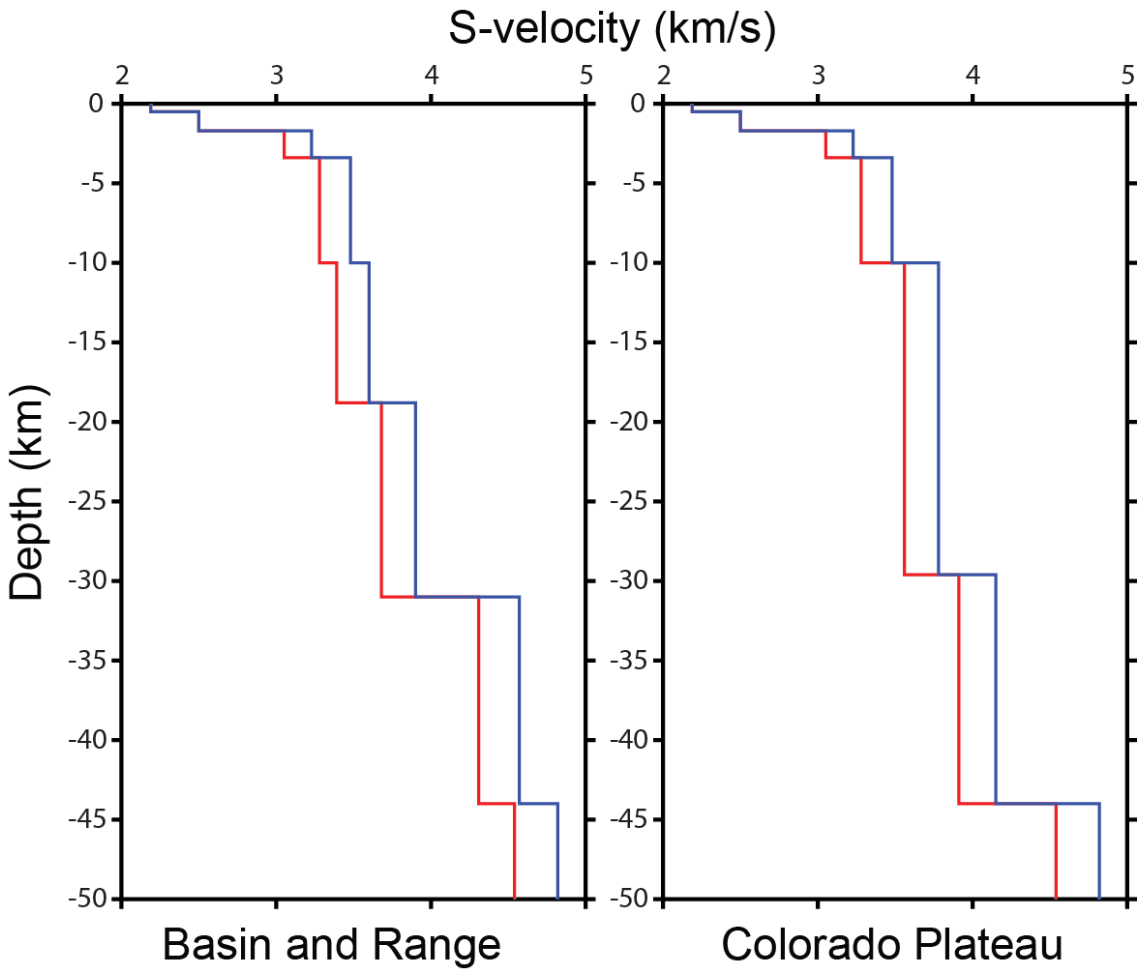

Figure 3. Final velocity models. New S-velocity models compared to starting models for the Basin and Range (left) and the Colorado Plauteau (right). Red lines show the starting model calculated using a Vp/Vs of 1.74. Blue lines show the new model calculated with a Vp/Vs of 1.64. The top two layers for both versions of each model are similar and are calculated using a Vp/Vs of 1.96.

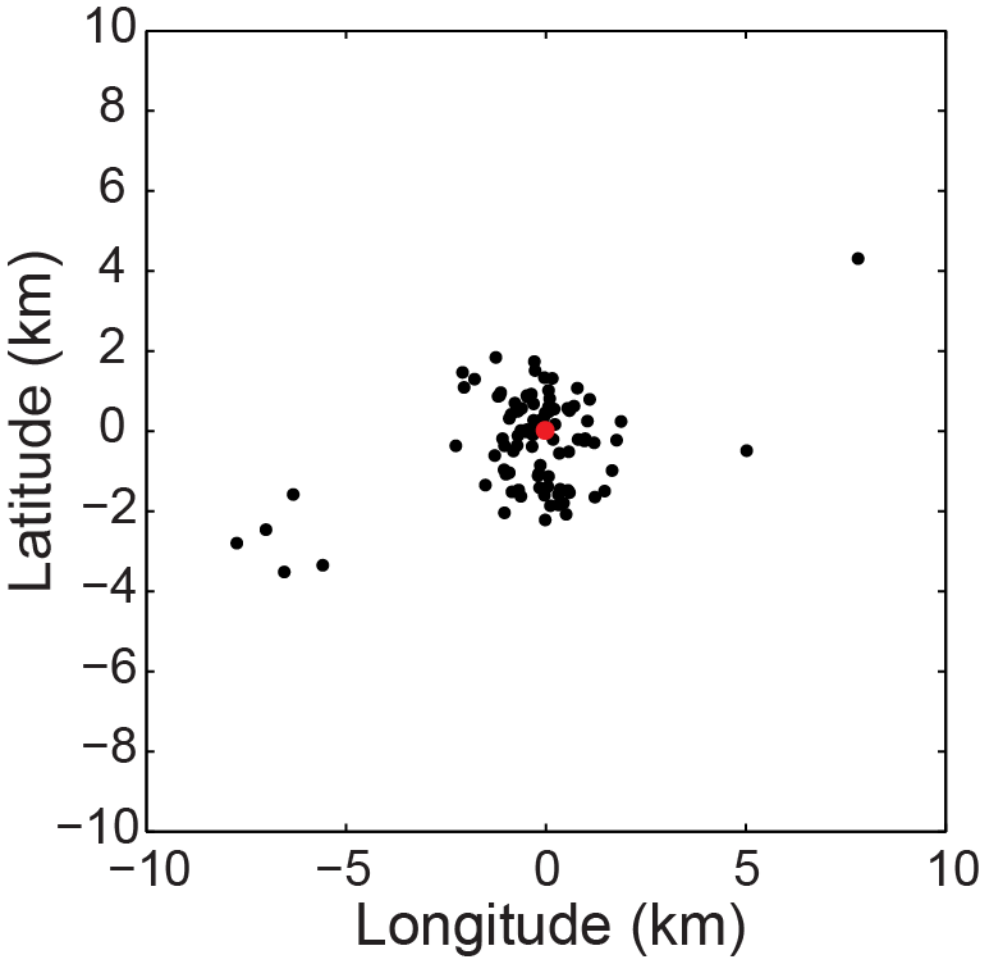

Figure 4. Initial locations. Locations of the Circleville earthquake sequence, using the revised velocity model. Locations are shown relative to the main shock location (red dot).

For the master-event method, the three events with well-constrained hypocenters were used to determine the optimal station delay to be subtracted from the arrival time of P-phases, as well as S-phases where available. The station delay corrects errors in the velocity model, particularly lateral variations in the upper crust and thus eliminating the need for distance weighting in the location procedure. The P- and S-phase delays are empirically chosen from the median residual among the master event residuals at each station and an initial input location calculated from the median longitudes, latitudes, and depths of the master events.

The first two master events occurred on January 10, 2011, and had coda magnitudes, $M_{C,}$ 1.5 and 1.8, respectively. The third and largest master event, M_w 3.8, occurred two days later on Jan. 12 and is a particularly valuable event because of its larger magnitude and the corresponding clarity of the phase arrivals. P-arrivals for all three master events were picked from a total of 16 stations, including the portable station. S-wave arrivals were picked on three 3-component broadband stations, CPS, MTPU, and TCRU, which are located approximately 3, 25, and 42 km from the master events, respectively. All events were relocated using HYPOINVERSE with the calculated station delays.

After master-event relocation, the average RMS decreased from 0.14 to 0.12 seconds and the median vertical uncertainty from 1100 to 1000 meters from the initial location results. The median horizontal uncertainties remain 400 meters. While the error improvement is small, there is some degree of clustering of the events although the hypocenters are still scattered (Figure 5). When viewed in cross-section facing

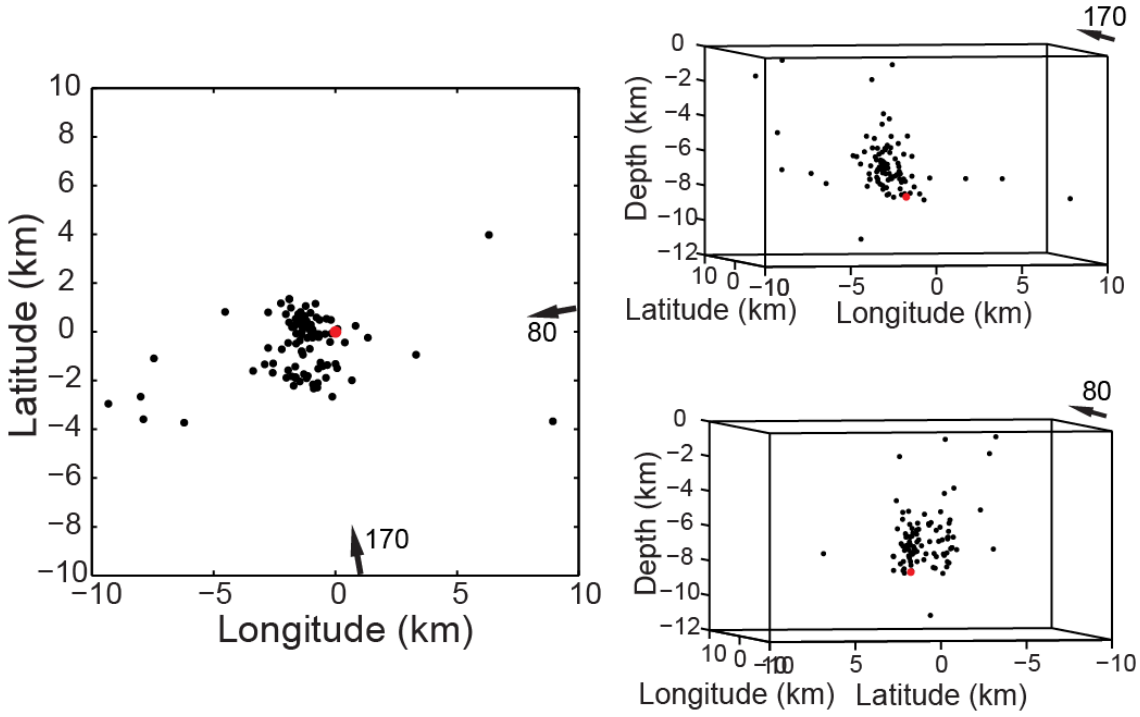

Figure 5. Master event relocations. Master event locations plotted in map view (left) and in cross-sectional view from 170° azimuth from north (upper-right) and 80° azimuth from north (lower-right). The latitude, longitude, and depth axis are given in kilometers and the mainshock (red dot) is the origin. The 170° view is looking northward into the seismicity as an observer standing at the bottom arrow on the map view. The 80° view is looking westward into the seismicity from the arrow on the side.

north along ~170° azimuth, the locations exhibit a small degree of planar clustering (Figure 5). After the master event relocations, the three master events are the best located events in the sequence, with horizontal errors between 200-300 meters and vertical errors between 200-400 meters, respectively. Having these well-located events allowed us to maintain location accuracy throughout the study and was the most significant contribution of the master event method. Furthermore, the revised hypocenters provide good starting locations for the double-difference method of *Waldhauser and Ellsworth* [2000].

2.3 HypoDD Relocations

HypoDD is a double-difference relative relocation method developed by *Waldhauser and Ellsworth* [2000]. HypoDD reduces location errors by minimizing the travel-time residuals at a common station for different events. Assuming that signals from closely spaced events travel the same ray path, the effects of path heterogeneities on travel-time are removed by using the travel-time differences between events. Ideally, the residual directly reflects the different locations of the events. By calculating this residual for each event pair, the entire sequence can be relatively relocated and velocity-model errors are minimized.

HypoDD uses P- and S-wave differential times from catalog travel-time differences between event arrivals and lag-times found from the cross-correlation of events. We used the program *ph2dt* [*Waldhauser and Ellsworth*, 2000] to process the observed and calculated phase arrival times reported by HYPOINVERSE from the

master event relocations and calculate all travel-time differentials. We also determined a set of cross-correlation lag-times to input into hypoDD.

To obtain the most accurate lag-times for closely located events, we only correlate the P-waves between events at broadband stations MTPU and TCRU (Figure 6). Prior to performing the P-wave cross-correlation, the waveforms were de-trended, tapered, band-pass filtered from 0.5-8 Hz using a second-order recursive Butterworth filter, and cut into windows of 3-4 seconds around the P-arrival so as not to include the S-arrival. All events in the mainshock/aftershock sequence were cross-correlated with respect to all other events (Figure 6).

We performed a simple clustering analysis on the cross-correlation results in order to determine what lag-time data to include in hypoDD. Using the clustering analysis functions in MATLAB, the events were linked according to their dissimilarity (one minus the correlation coefficient) with all the other events (Figure 7). The events were clustered based on a dissimilarity distance of 0.2, and lag-times from the largest cluster were included in the inversion. Figure 7 demonstrates how the dissimilarity distance determines the clustering of events. At each point where the line corresponding to 0.2 cuts across a 'stem', all events connected to the stem below 0.2 become an individual cluster where the largest cluster is delineated by the red box (Figure 7).

Ten input parameters must be specified to use hypoDD to relocate events (Tables 1-2). The number of iterations must be specified and can be grouped into sets using different parameters. P- and S-arrival times can be weighted differently as can the lag-times. WTCCP and WTCTP control the weights for the P-wave lag-times and

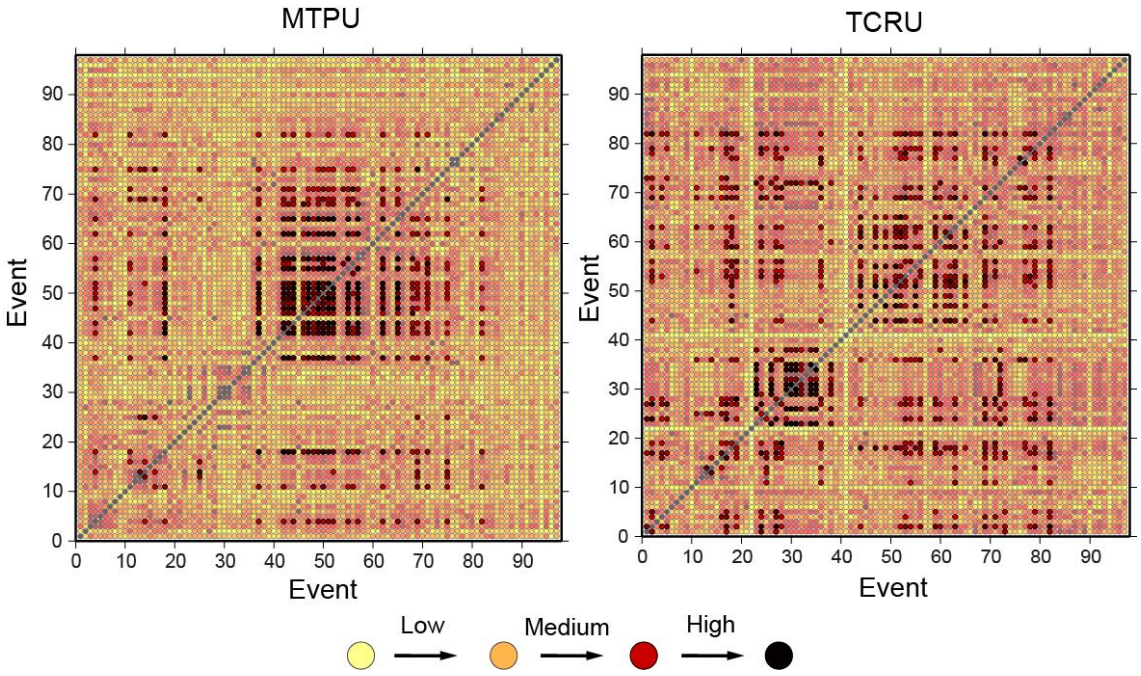

Figure 6. Cross-correlation results. Station results of cross-correlation analysis of P-waves recorded at MTPU (left) and TCRU (right). Event pairs whose lag-times were used in hypoDD are more darkly shaded.

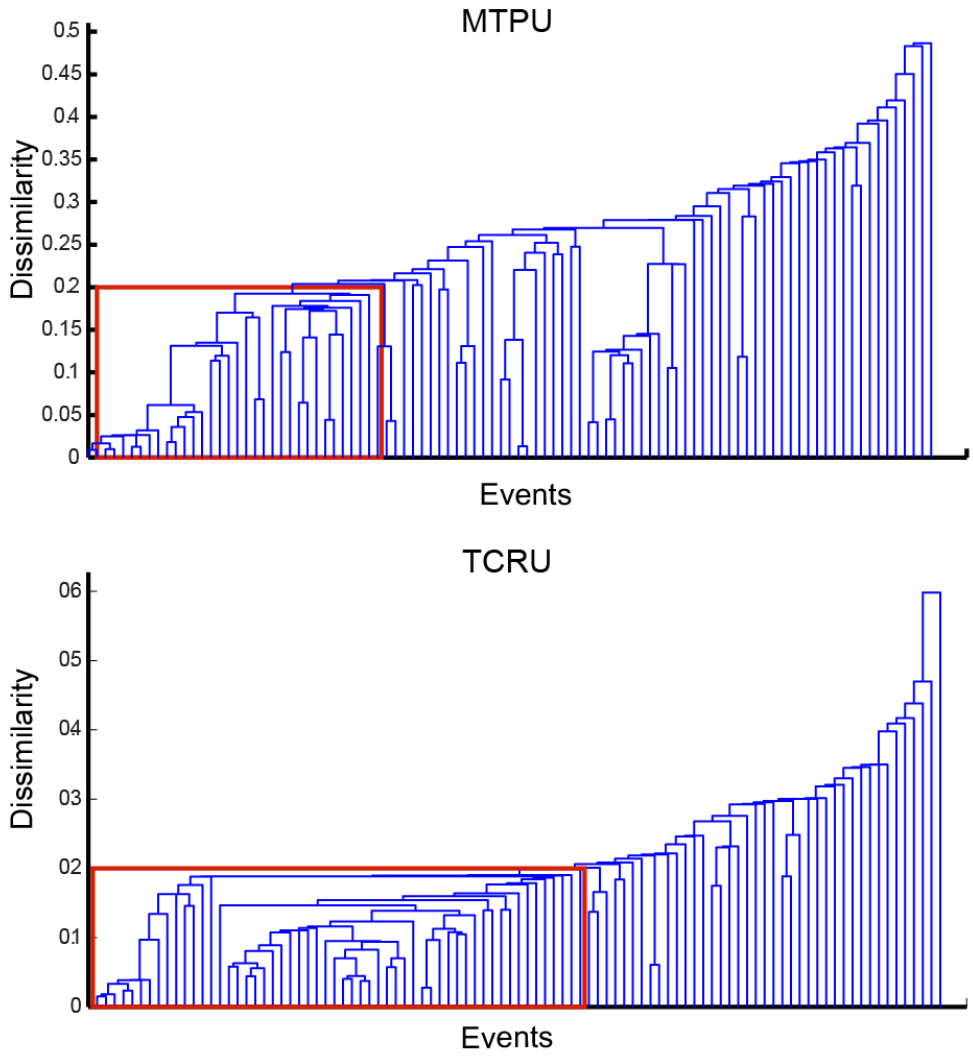

Figure 7. Station dendrograms. Station dendrograms showing the dissimilarity clustering results for Stations MTPU (top) and TCRU (bottom). Dissimilarity is measured by subtracting the event pair cross-correlation coefficient from one. Events are clustered based on a value of 0.2, where all events linked at smaller values become clustered together. Red box indicates the largest cluster.

Table 1. HypoDD parameters for catalog-only inversion

Iteration	WTCCP	WTCCS	WRCC	WDCC	WTCTP	WTCTS	WRCT	WDCT
1-5	-	-	-	-	1.0	0.5	-	2.0 km
5-10	-	-	-	-	1.0	0.5	-	2.0 km
10-15	-	-	-	-	1.0	0.5	6	2.0 km

Not all parameters require inputs for the inversion to proceed, and parameters marked by a dash were not used in the inversion. In this inversion schema, P and S differential time were weighted the same for each set of iterations.

Table 2. HypoDD parameters for final inversion

Iteration	WTCCP	WTCCS	WRCC	WDCC	WTCTP	WTCTS	WRCT	WDCT
1-5	0.1	-	-	2.0 km	1.0	0.5	-	2.0 km
5-10	1.0	-	-	2.0 km	0.1	0.05	-	2.0 km
10-15	1.0	-	6	2.0 km	1.0	0.5	6	2.0 km

Not all parameters require inputs for the inversion to proceed, and parameters marked by a dash were not used in the inversion. In this inversion schema, P and S differential time and lag-time weights change depending on the set of iterations. For the first set, differential times are the primary relocation data; in the second, lag-times are the primary data used; and in the third, lag-times and differential times are given equal consideration.

catalog times, respectively. Likewise, WTCCS and WTCTS control the S-wave cross-correlation and catalog weights. WRCC and WRCT are the cross-correlation and catalog standard deviations beyond which outliers are removed. WDCC and WDCT are the most important parameters as these are the cross-correlation and catalog event linking distance. HypoDD clusters data based on spatial similarity; therefore, any event not within the WDCC/WDCT distance of another events is not included in a cluster. HypoDD can produce multiple clusters, but the WDCC/WDCT value is applied to all. Lastly, a damping value is specified when run as a least-squares inversion. HypoDD accepts one velocity model as input. HypoDD can be run as a regularized least-squares inversion or an SVD inversion, depending on the size of the data set.

HypoDD was run under different conditions in order to observe the stability of the locations derived with such a small dataset as well as the effects of the addition of cross-correlation lag-times. For each dataset, catalog times for all available events since 1981 for the region based on a 10 km radius around the epicenter of the January 2011 mainshock were incorporated into hypoDD to help stabilize the inversion. The inclusion of historical seismicity into the catalog resulted in 241 usable events. Because of the small size of the final catalog, singular value decomposition (SVD) was judged to be the optimal method to use given that hypoDD reports calculated errors for SVD, unlike the least-squares inversion method. In addition, all hypoDD inversions used the final CP model because the sequence occurred in that region.

First, we only used P- and S-wave catalog differential times to relocate the events using the parameters shown in Table 1. The results consist of one large cluster containing 73 final events with improved, more tightly clustered locations. To further

improve the relocations, lag-times determined from the cross-correlation of events were included in the hypoDD analysis.

We included lag-times from the largest cross-correlation (Figure 6) with coefficients >0.7 that were among the 73 events in the first hypoDD result to insure that only high-quality lag-times were used. Including lag-times produced more tightly clustered locations (Figure 8) than when only using catalog differential times, with a significant number collapsing onto what appears to be a near-vertical plane with an ~170° strike (Figure 8).

Because hypoDD does not place events in absolute space, to determine absolute locations,a we calculated the vector difference between the M_w 3.8 aftershock hypoDD and master event locations. The M_w 3.8 master event was chosen as the reference point because it is the most reliably located event in the catalog. Using this vector, all events were shifted in space to the final locations.

While the SVD hypoDD inversion method should yield meaningful errors, we performed two jackknife analyses following the example of *Waldhauser and Ellsworth* [2000] by removing one event at a time and one station at a time and re-performing the inversion. This procedure identifies the events that are likely to have the greatest change in location and that affect locations the most, and indicates whether any particular station has a disproportional impact on the relocation process. All of the resulting relocations were compared to a control, in this case, the final hypoDD solution. In order to accurately compare location changes, the relocated M_w 3.8 master event was shifted to its initial location and, for each run, that same shift was applied to all of the relocations.

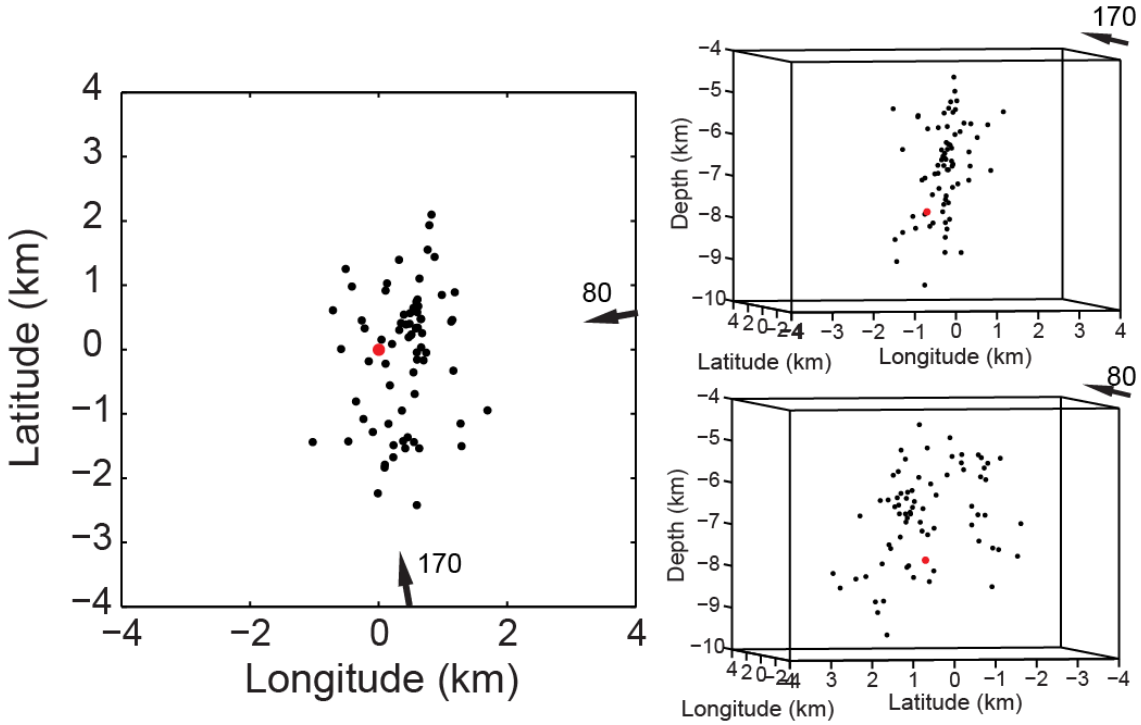

Figure 8. Final locations. Final hypoDD locations for 73 events are plotted in map view (left) and in cross-sectional view from 170° azimuth from north (upper-right) and 80° azimuth from north (lower-right). Latitude, longitude, and depth axes are in kilometers and the mainshock (red dot) is the origin. The 170° view is looking northward into the seismicity as an observer standing at the bottom arrow on the map view. The 80° view is looking westward into the seismicity from the arrow on the side.

After removing events, we analyzed the data in two different ways. The first way was by individual events to observe the change in location of each event as a result of the jackknife, and the second was by the differences in the entire sequence from each jackknife run to see how each event affected the relocation process. Analysis of the station jackknife indicated whether or not any station had a significant bias in the location process. The changes in locations were observed to be consistent among the different analyses.

The SVD yielded location uncertainties in the range of 20-100 meters. However, the changes in locations from the jackknife analysis were larger. The average horizontal error from the jackknife was approximately 200 meters, down from 400 meters from the master event relocations. Overall, 95% of the horizontal location changes are less than 500 meters. The collective horizontal change from the jackknife is shown in Figure 9 and is plotted with respect to both distance and azimuthal change. The vertical errors are still larger than the horizontal errors after hypoDD, with fewer than 10% of the location changes being greater than 1000 meters (Figure 9). After the master event relocations, 50% of reported errors were greater than 1000 meters. Therefore, hypoDD resulted in a large improvement in location quality and the reduction of location uncertainties. Despite the errors determined from the jackknife, the geometry appears to be stable between individual inversions. This will be further discussed in the next section using principal component analysis. Furthermore, the station jackknife indicated no obvious location bias from any one station on the location results.

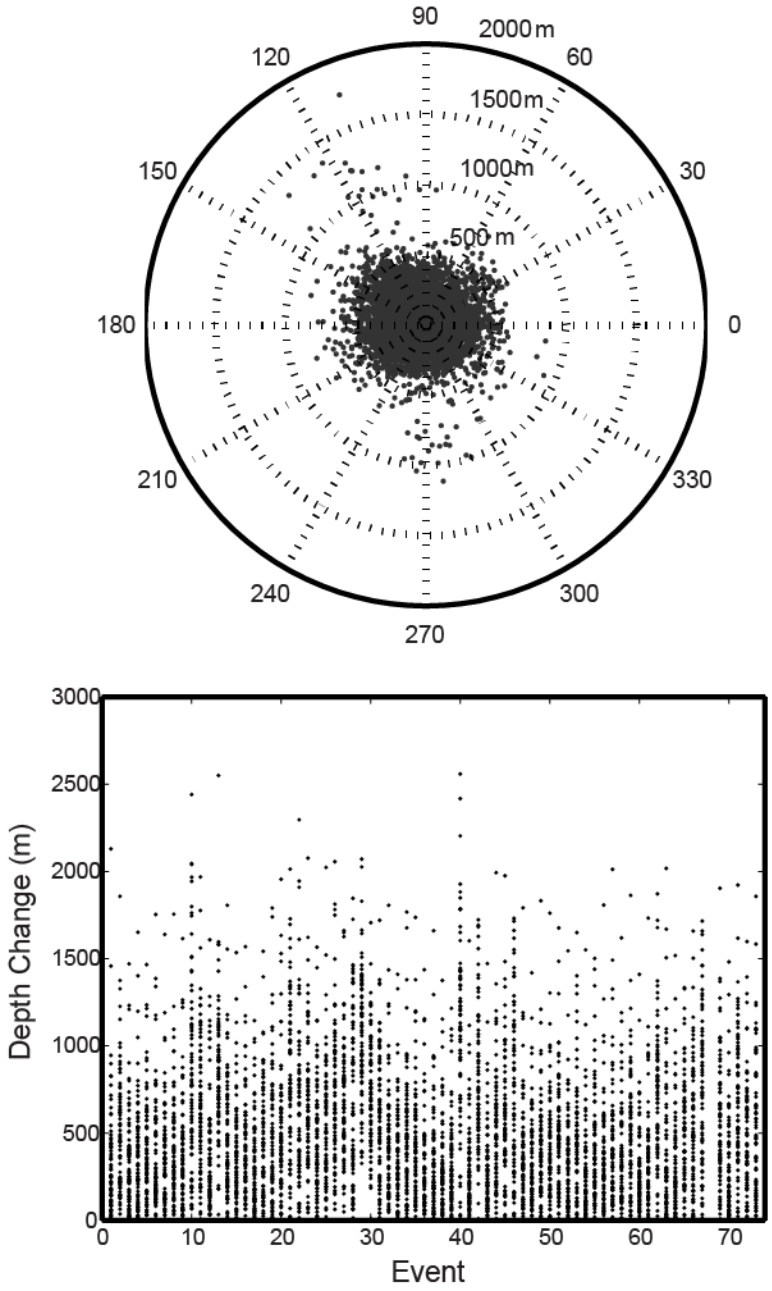

Figure 9. HypoDD error analysis. Location errors from the hypoDD jackknife analysis (upper) plotted in polar coordinates to show azimuthal change as well as distance. The 500 meter radius corresponds to 95% inclusion value. Depth errors (lower) where the 90% inclusion value is 1000 meters.

CHAPTER 3

FAULT GEOMETRY

3.1 Principal Component Analysis

The overall geometry of the seismicity can be evaluated visually when observed in different cross-sectional views, but this method is qualitative. Given the horizontal and vertical location uncertainties of 500 meters and 1000 meters, quantifying the geometry in terms of hypocenter locations and pattern, as well as its stability, becomes important. *Michelini and Bolt* [1986] and *Shearer and Hardebeck* [2003] use the method of principal component analysis to help define hypocenter geometries. Principal component analysis (PCA) is a statistical approach to quantifying the spread of the data, specifically the locations in this case, indicating whether the data cluster along a line or a plane or form a sphere. Because the locations are in a three-dimensional, *xyz* coordinate system, three orthogonal principal axes oriented in the directions of greatest and least spread, or variance, and a third direction of intermediate spread can describe the spatial pattern of the data in terms of a best-fitting ellipsoid.

Principal component analysis is done by performing an Eigen-decomposition of the covariance matrix of the location data. The resultant eigenvectors describe the orientations of the principal axes and the eigenvalues describe the magnitude of each axis. The covariance matrix, **V**, is a 3 x 3 matrix found using equation (1),

$$V_{ij} = \frac{1}{m}\sum_{k=1}^{m}\left(x_i^k - \bar{x}_i\right)\left(x_j^k - \bar{x}_j\right) \qquad i,j = 1,2,3, \tag{1}$$

where m is the number of observations and $\bar{x}_i$ is the mean of each variable. The resultant eigenvalues are denoted as λ_1, λ_2, and λ_3 where $\lambda_1 > \lambda_2 > \lambda_3$ and the corresponding eigenvectors are U_1, U_2, and U_3.

If $\lambda_1 \approx \lambda_2 \approx \lambda_3$, the spatial pattern is approximately spherical. If λ_1, $\lambda_2 >> \lambda_3$, the locations cluster around a plane, which is a typical result for mainshock/aftershock seismicity. Planarity can also be quantified using equation (2)

$$planarity = 1 - \frac{2\lambda_3}{\lambda_1+\lambda_2} \tag{2}$$

where a result of 1 is completely planar and 0 is spherical. Lastly, if $\lambda_1 >> \lambda_2$, λ_3, the events cluster along one axis such that the geometry is linear, where linearity can also be quantified using equation (3)

$$linearity = 1 - \frac{\lambda_2+\lambda_3}{2\lambda_1} \tag{3}$$

where l is completely linear. As the eigenvalues describe the magnitude of the axes, the lengths can be determined by taking the square root of each value to obtain the radial length and multiplying by 2 to obtain the full length of each axis.

We applied the PCA method to the final locations and found λ_1=1.55, λ_2=0.737, and λ_3=0.201, where the planarity=0.82, indicating a planar solution. Figure 10 is a 2D

projection of the best-fitting ellipse to a map view of the data. The major axis has a length, L, of 2500 meters and minor axis has a width, W, of 1700 meters. The length/width ratio is 1.45, indicating a rectangular plane. The length is approximately the 150% of the width value.

In the case of seismicity clustered about a plane, the direction with the smallest variance is the normal to the plane. The inverse of equation (4) allows the strike and dip of the seismicity plane to be calculated in the initial coordinate system. Using the third eigenvector from the above results as the normal, the strike of the earthquake sequence is 190° and the plane dips 78° to the west.

To test the stability of the PCA calculation, a bootstrap with replacement analysis was applied to the final location data. Both the strike and dip, 190° and 78°, were observed to have errors of +/- 4° at a 1σ confidence interval, indicating no significant outliers. The planarity averaged 0.83 +/- 0.04 at 1σ confidence. To test the stability of the actual geometry, PCA was performed on the results from the different jackknife scenarios used to assess the errors in the hypoDD analysis to observe if the geometry changed significantly under different relocation scenarios. The average strike and dip were found to be 188° and 80°, respectively, with 1σ errors of less than 3°; likewise, planarity was calculated to be 0.78 +/- 0.03. Therefore, the geometry appears to be stable throughout the relocation jackknife.

PCA is often applied to seismic clusters within a catalog [*Michelini and Bolt*, 1986; *Shearer and Hardebeck*, 2003] to characterize different areas of seismicity. Such a method could potentially be applied to this sequence. However, because the number of data points decreases when the catalog is subdivided, problems may arise by over-

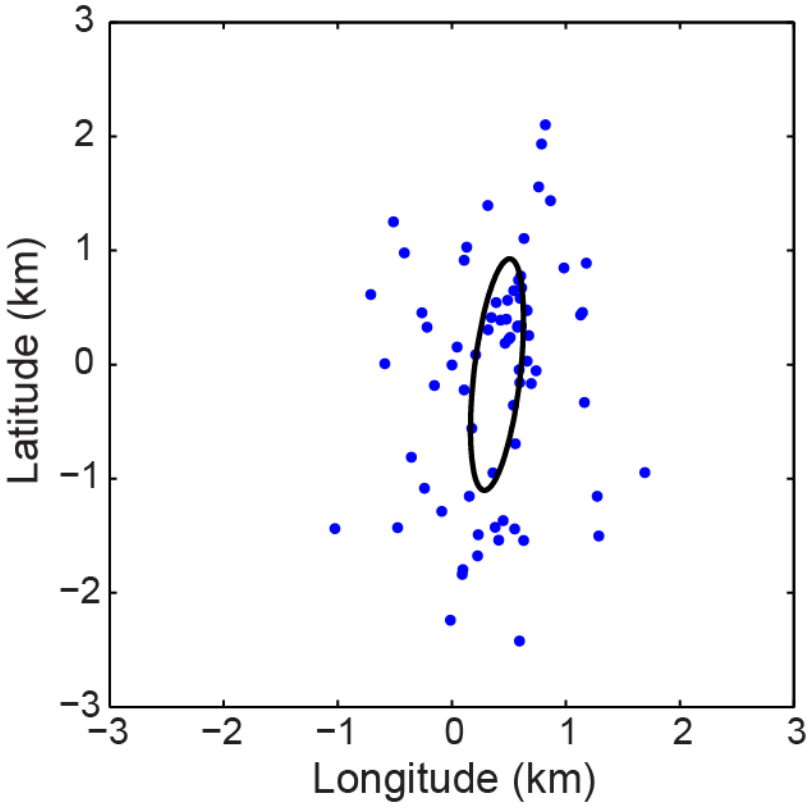

Figure 10. Best-fitting PCA ellipse. 2-D projection of the best fitting ellipse determined from PCA analysis plotted in map view. Note the ellipsoid is dipping at 79°; therefore, the projection of the ellipse appears smaller than it actually is.

dividing the catalog and trying to accurately analyze each subset with too few data points.

3.2 First Motion Focal Mechanisms

First motion focal mechanisms were determined for events with eight or more polarity picks, regardless of magnitude. The program HASH [*Hardebeck and Shearer*, 2002] is used for the plane-fit calculations because it allows for and, to some extent, accounts for the uncertainty in locations. The initial azimuths and take-off angles utilized by HASH were first calculated in HYPOINVERSE using a fixed depth set to the hypoDD determined depth for each event, and HASH was allowed a 1000 meter error in starting depth, consistent with the results from hypoDD. Because many of the arrivals are emergent, picking first motions is difficult and the events are typically small, so fewer stations are available at distances greater than 200 km. To account for associated errors as well as station issues, HASH was allowed to consider 10% of the station polarities to be reversed when calculating possible focal planes from fifty trials from which a preferred mechanism was determined. Because HASH varies the depth within the error bounds and recalculates take-off angles, the take-off angles determined from HYPOINVERSE were checked against the final mechanism.

First-motion focal mechanisms were resolvable for 8 events with magnitudes less than 3.2. The information for each event is listed in Table 3, and the locations are shown in Figure 11. Conclusions are difficult to draw given the variety of mechanisms present, particularly in conjunction with depth and magnitude. Several of the events (#5-9) occurred very close together in time, and had clearer arrivals from lower cultural

noise at night. Right-lateral strike-slip mechanisms appear to be common, particularly as oblique events have a strike-slip component. Furthermore, while the strike-slip results appear to be consistent, first-motion focal mechanisms are difficult to determine precisely, and all the results contain uncertainties in exact plane locations though the mechanism tend to remain the same.

3.3 Moment Tensor Plane Comparisons

Four events were large enough to obtain moment tensor focal mechanism solutions [*Whidden and Pankow*, 2012]. The mainshock was a normal-slip event with an Mw of 4.5, and the largest three aftershocks included a Mw 3.4 strike-slip and Mw 3.4 and Mw 3.8 normal events that occurred on January 6, 7, and 12, respectively. All four moment tensors, as well as six of the first motion focal mechanisms (Table 3), contained a focal plane with a strike between 160° and 180°, two at precisely 170°, but the dips ranged from 18° westward (January 12 normal event) to 72° eastward (January 6 strike-slip event). The eight focal mechanism planes, two from each mechanism, provide eight potential fault orientations to relate to the data.

To observe how the locations relate to the eight planes, the strikes and dips of each plane were converted to a normal vector via equation (4) from *Stein and Wysession* [2003]

$$\hat{\boldsymbol{n}} = \begin{bmatrix} -sin\delta sin\theta \\ -sin\delta cos\theta \\ cos\delta \end{bmatrix}, \tag{4}$$

Table 3. Summary of first motion focal mechanisms

Number	Date	Depth (km)	Magnitude	Mechanism	N-S plane?
1	2011/01/0312:26.58	6.9	2.8	Oblique-normal	yes
2	2011/01/03 14:05.26	7.4	1.1	Strike-slip	yes
3	2011/01/03 15:38.06	6.5	2.4	~Strike-slip	yes
4	2011/01/03 20:23.44	7.3	3.1	Strike-slip	yes
5	2011/01/03 21:04.14	4.8	1.8	Strike-slip	yes
6	2011/01/03 22:37.44	7.2	1.9	Oblique-normal	~yes
7	2011/01/04 03:43.16	5.8	1.7	Oblique-normal	no
8	2011/01/04 19:52.58	7.5	2.0	Strike-slip	no

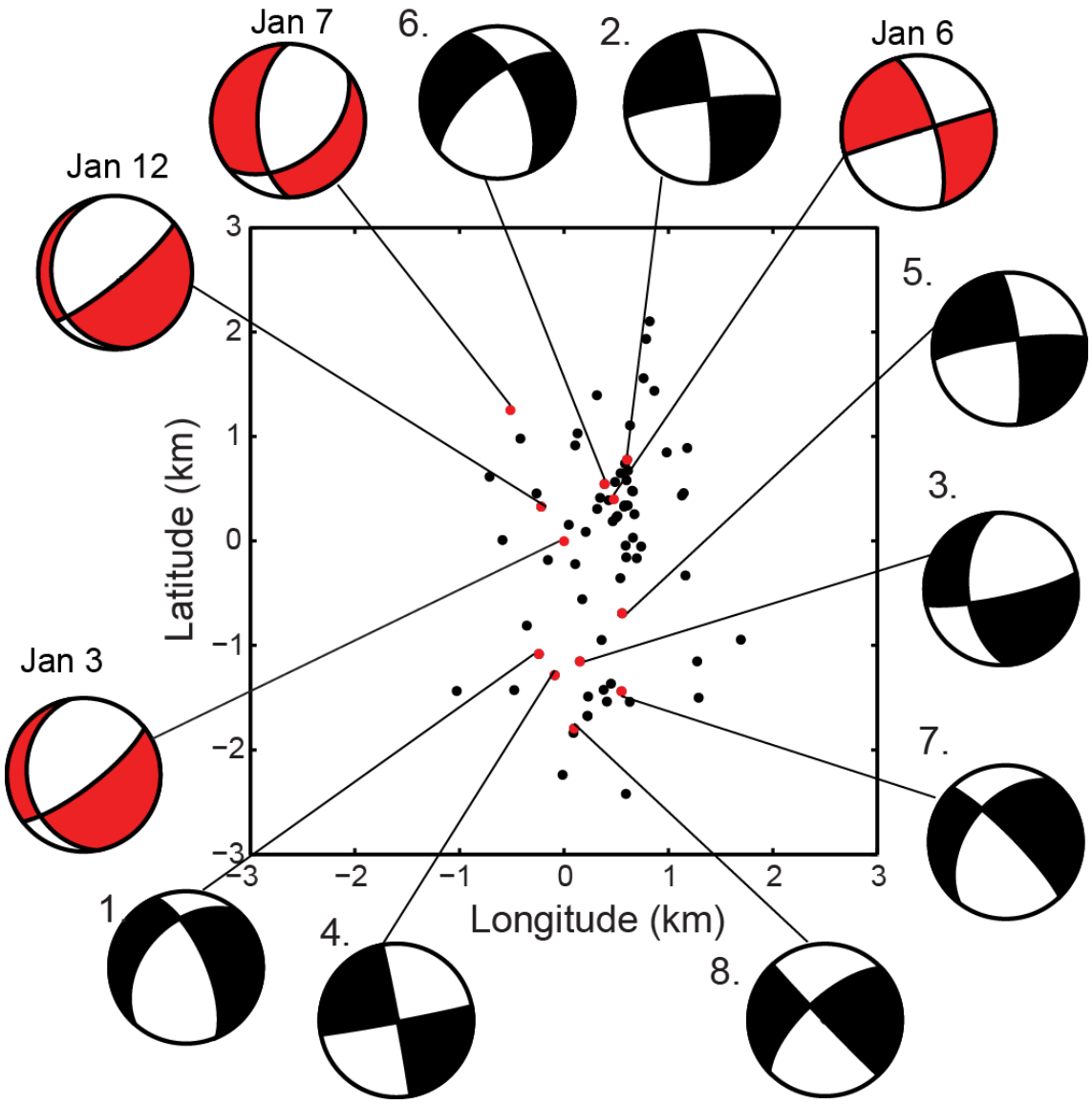

Figure 11. Focal mechanism map. First-motion (black) and moment-tensor (red) focal mechanism results plotted in map view. See Table 3 for more detailed information.

where δ is dip angle and θ is the strike azimuth. Using the plane normal and the earthquake hypocenter to give it an absolute spatial location, the distance between each point and the focal plane can be calculated. The calculation was performed for each of the eight planes with respect to all events in the sequence and the events located within 500 meters (the hypoDD error bound) of the plane is considered to "fit" or to potentially have occurred on the plane.

Using the moment tensor from *Whidden and Pankow* [2012], the main-shock focal mechanism has a west-dipping low-angle plane and a northeast-southwest striking, near-vertical plane (Figure 12). The near-vertical plane, when compared to the data, only aligns to a few data points as it cuts across strike, but the low-angle plane "fits" a number of deeper events along strike that appear to be dipping to the west (Figure 12). The focal mechanism for the strike-slip event that occurred on January 6 has two steeply dipping planes, one striking north-south and the other east-west (Figure 13), and it is the shallowest of the four events. Like the mainshock mechanism, the east-west plane runs across strike and only "fits" a small section of data, whereas the largest number of events aligned to any plane in this analysis corresponds to this particular ~170° north-south trending plane (Figure 13). The third large event with a focal mechanism occurred on January 7. This event is the deepest, and has two moderately dipping planes that strike north-south and east-west (Figure 14). Like the two other events, the east-west plane for this event also does not match the data, particularly as only one event is considered close enough; however, the north-south striking plane does capture a good portion of the data, but whether it is coincidence remains to be seen. Lastly, the large aftershock on January 12 is similar to the

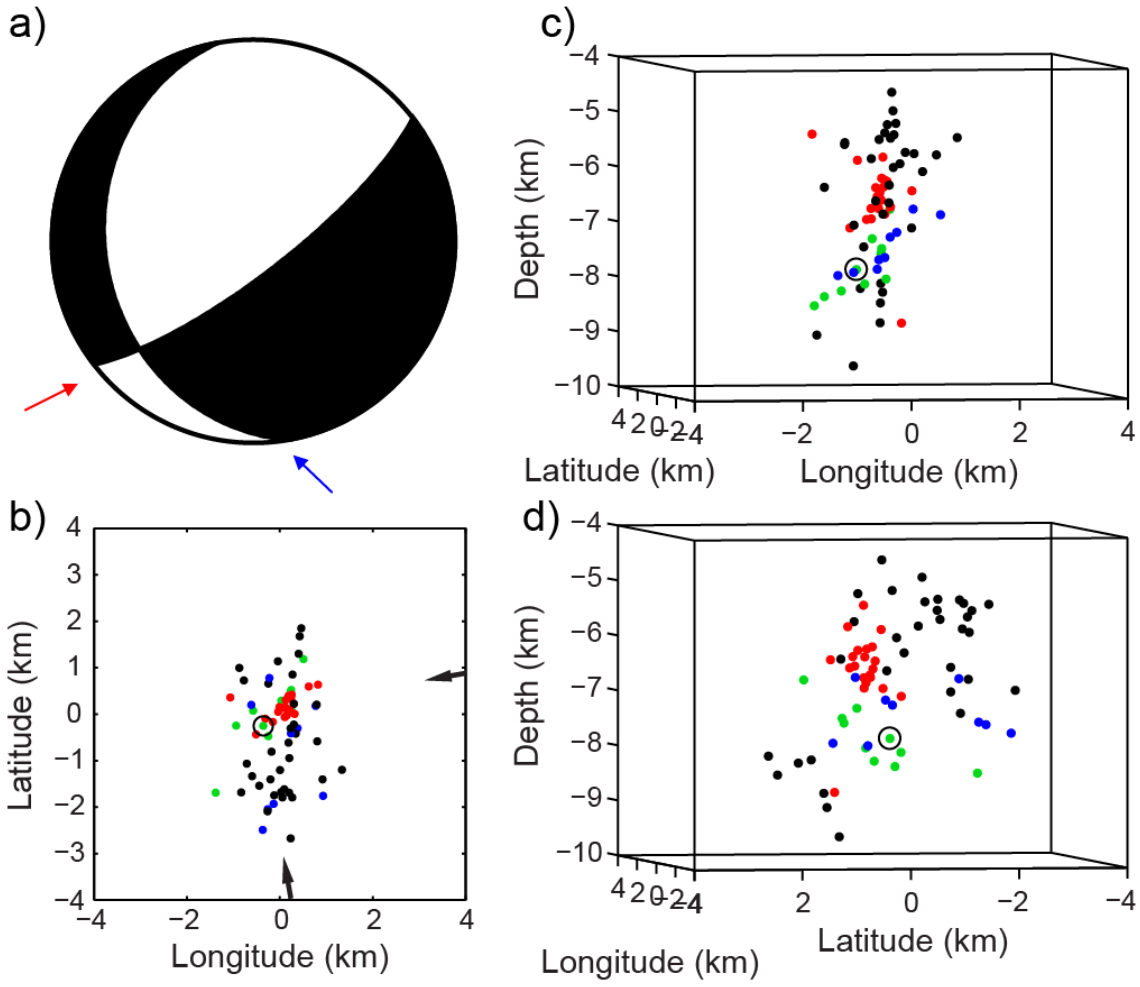

Figure 12. Mainshock plane comparison. The mainshock (black circle) moment tensor is a) plotted in lower hemisphere view, and the locations are plotted in b) map view, c) 170° cross-sectional view, and d) 80° cross-sectional view. The relation of the N-S focal plane (blue arrow) to the data (blue dots) and the relation of the E-W plane (red arrow) to the data (red dots) can be observed. Some locations are close to both planes (green dots), and others fall outside of both (black dots).

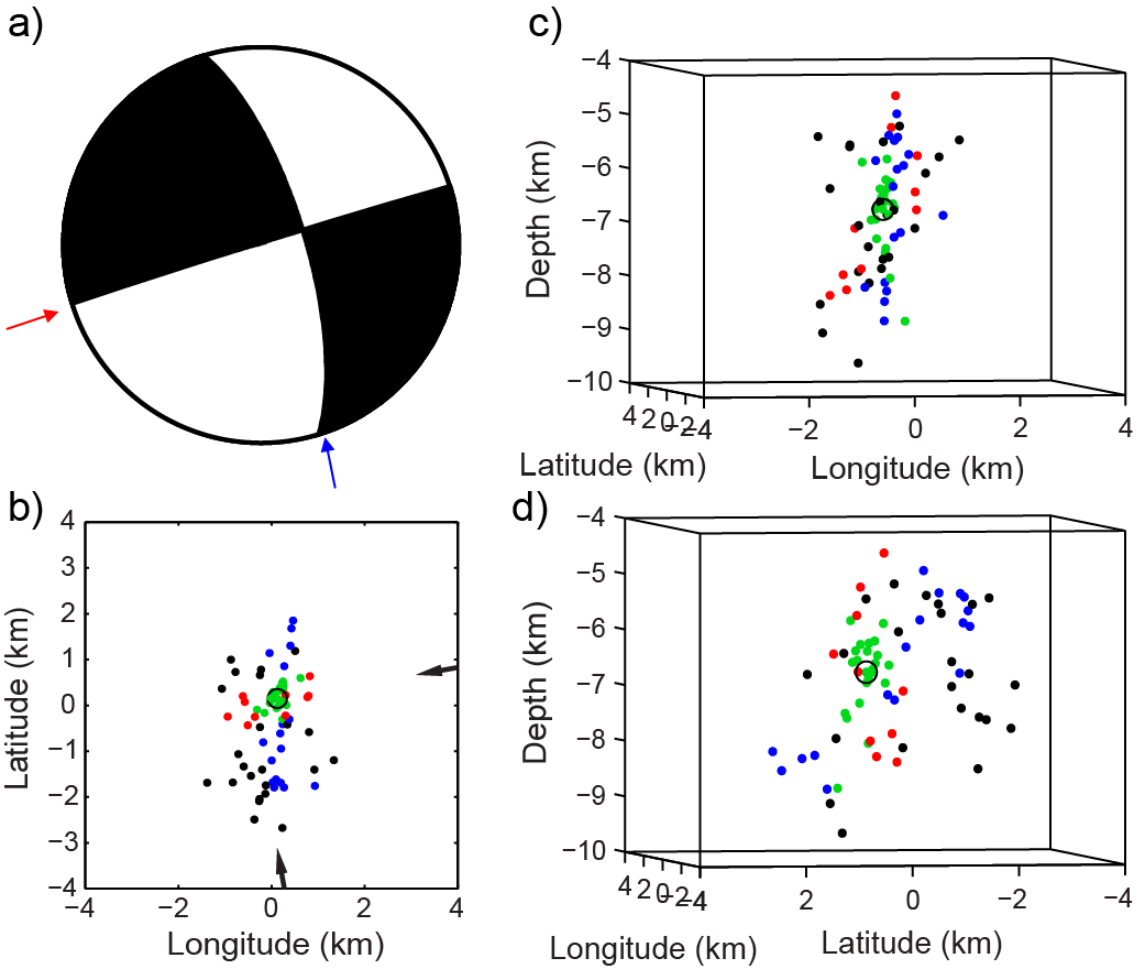

Figure 13. Strike-slip aftershock plane comparison. The mainshock (black circle) moment tensor is a) plotted in lower hemisphere view, and the locations are plotted in b) map view, c) 170° cross-sectional view, and d) 80° cross-sectional view. The relation of the N-S focal plane (blue arrow) to the data (blue dots) and the relation of the E-W plane (red arrow) to the data (red dots) can be observed. Some locations are close to both planes (green dots), and others fall outside of both (black dots).

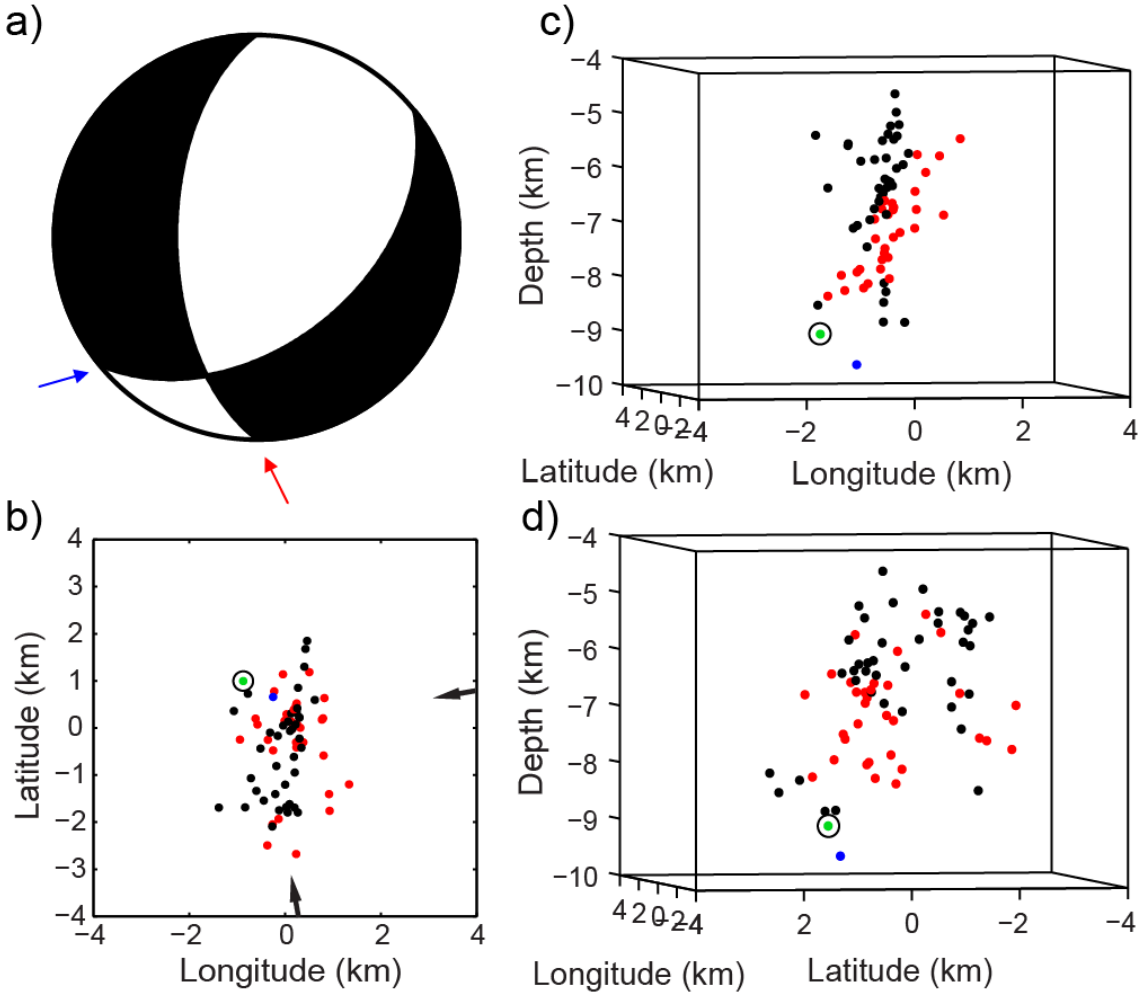

Figure 14. January 7 aftershock plane comparison. The mainshock (black circle) moment tensor is a) plotted in lower hemisphere view, and the locations are plotted in b) map view, c) 170° cross-sectional view, and d) 80° cross-sectional view. The relation of the N-S focal plane (red arrow) to the data (red dots) and the relation of the E-W plane (blue arrow) to the data (blue dots) can be observed. Some locations are close to both planes (green dots), and others fall outside of both (black dots).
mainshock except that the north-south trending plane dips more shallowly (Figure 15).

the results are similar to those of mainshock as the events are closely located at depth, and, once again, the low angle plane appears to be best fit to the data (Figure 15).

Upon visual inspection of the results in Figures 12-15, the northeast-southwest striking planes do not appear to align well with the aftershock locations, whereas the north-south plane in each focal mechanism does, although the planes align to different areas of the data as expected from the wide range of dips. Interestingly, the normal events, mainshock included, were located deeper than the strike-slip event. To consider the possibility that ruptures could have occurred on two planes, the ~170° striking planes from the mainshock and the strike-slip event were compared to the data (Figure 16). Visual inspection suggests that the two planes fit the data quite well, and two rupture planes are certainly possible.

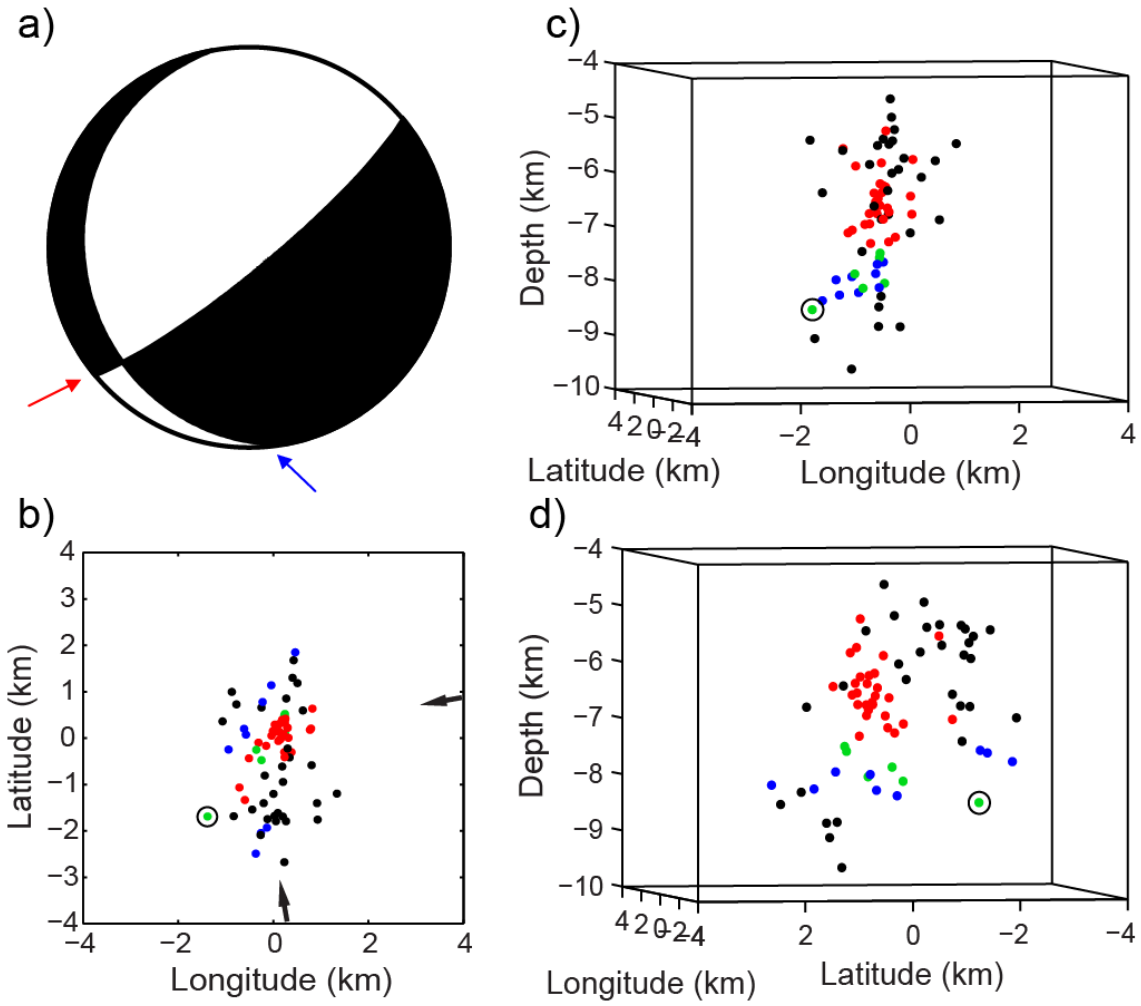

Figure 15. January 12 aftershock plane comparison. The mainshock (black circle) moment tensor is a) plotted in lower hemisphere view, and the locations are plotted in b) map view, c) 170° cross-sectional view, and d) 80° cross-sectional view. The relation of the N-S focal plane (blue arrow) to the data (blue dots) and the relation of the E-W plane (red arrow) to the data (red dots) can be observed. Some locations are close to both planes (green dots), and others fall outside of both (black dots).

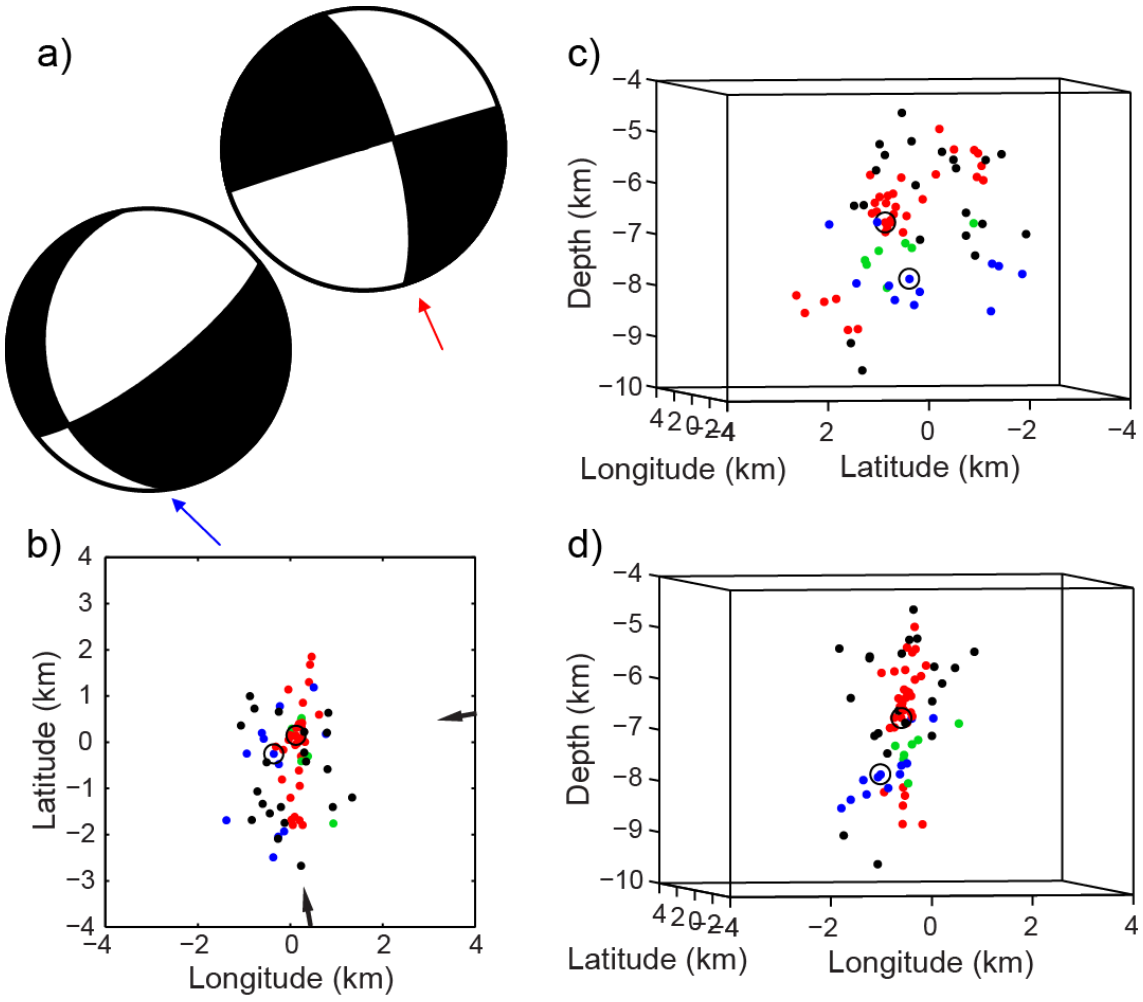

Figure 16. Comparison of two 170° striking planes. Two different 170° striking planes, one from the main shock (blue) and one from the strike-slip aftershock (red), are applied to the data as in Figures 12-15. The color convention between planes and locations is the same as in Figures 12-15.

CHAPTER 4

SOURCE CHARACTERISTICS

4.1 Empirical Green's Functions

For many events with moment tensor solutions, a Green's function, which describes the earth response to an impulse, is not resolvable, particularly in local cases where the seismogram is enriched in high-frequency energy. In such cases, a nearby aftershock or foreshock with waveforms highly similar to the earthquake of interest can be used as an empirical Green's function, or EGF, for the main event [*Hartzell*, 1978]. Typically, an EGF would be approximately two magnitudes smaller than the mainshock as such a small event is, by comparison, a point source with a delta function response that can be deconvolved from the mainshock, theoretically removing the earth response and leaving the source-time function (STF) of the mainshock observable with a positive amplitude on the seismogram.

The cross-correlation and cluster analysis established to determine event lag-times was also used to select potential events to use as EGFs for both the mainshock and the strike-slip aftershock. Care must be taken when picking events within clusters as the linking routine can result in two end-member events that are not highly correlated; hence, the correlation coefficient needs to be considered when determining

event pairs. Waveforms for potential EGFs must also be visually inspected at different stations (Figure 17) to ensure that the correlation holds azimuthally and is not a local effect at a single station. Only the two nearby broadband stations, MTPU and TCRU, were viable options for checking correlations because all other close stations that recorded the mainshock and first aftershock were single-component short period instruments that produced clipped waveforms. Seismograms used for EGF deconvolution must have a high signal-to-noise ratio in order to resolve an STF. Close stations (MTPU and TCRU) are typically used because the strength of the seismic signal is large enough for the record to meet this requirement. However, in this situation, a third station, SRU which is located at a distance of approximately 180 km, was also used.

One event was identified as a potential EGF for the mainshock (Figure 17) and two for the strike-slip event (Figure 17). The EGF for the mainshock was the second aftershock, which was located approximately 1.2 km away and, occurred less than 20 minutes after the mainshock. The EGF has a coda magnitude of ~1 compared to the mainshock M_w of 4.5. The first EGF (M_C 1.2) for the strike-slip aftershock (M_w 3.4) occurred two days before and was located ~1.5 km away almost directly above the aftershock. The second EGF (M_C 1.8) for the strike-slip event occurred at a greater distance, ~2.5 km, and occurred four days after. For these events, velocity records were converted to displacement and high-pass filtered at 1 Hz to remove the effects of integrating long-period noise in the velocity records for the smaller events.

The events are cut around the SH-wave and the EGFs are removed from the mainshock and strike-slip aftershock using a water-level (0.1) deconvolution

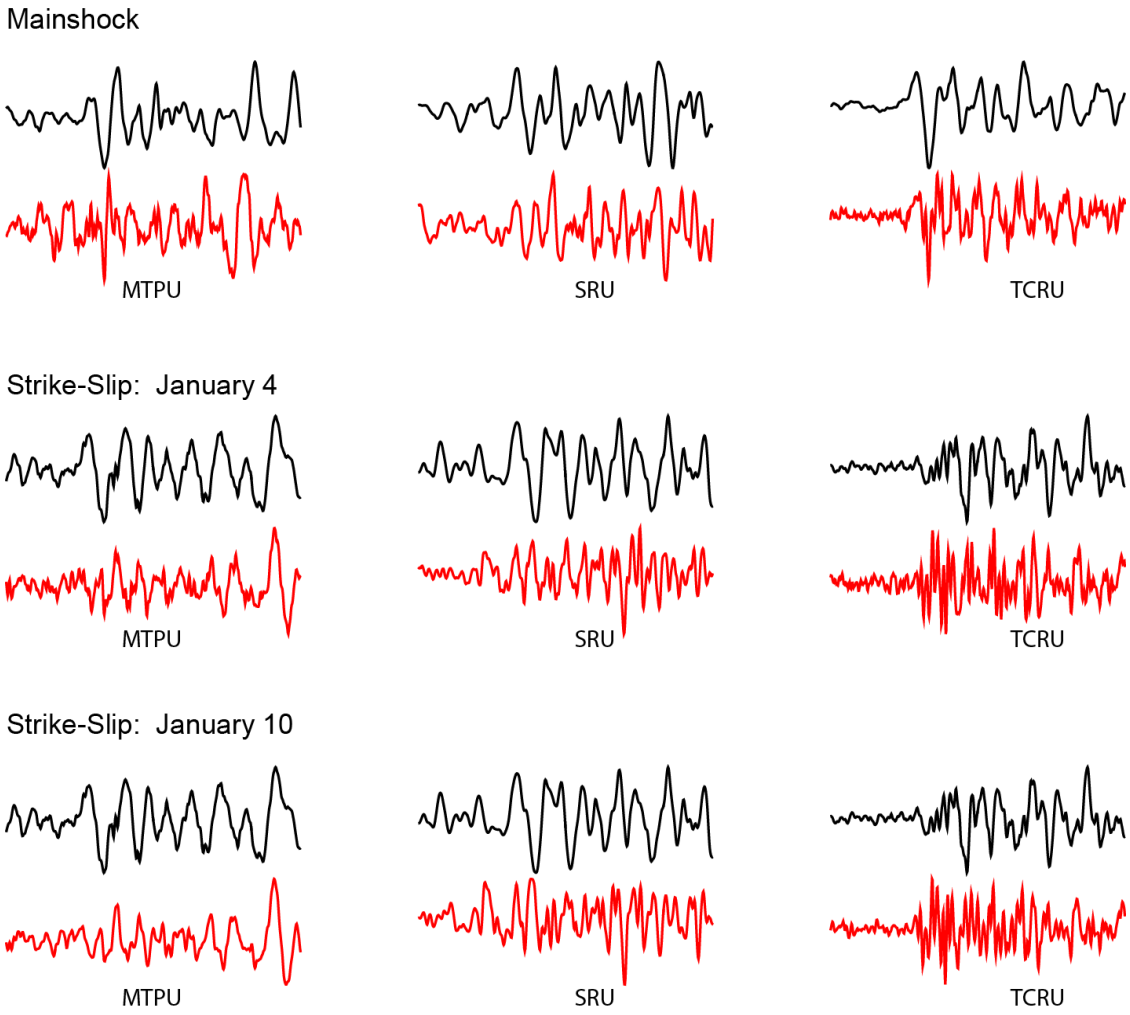

Figure 17. EGF waveform comparisons. Waveform comparisons for the mainshock and its January 3 EGF, the strike-slip aftershock and its January 4 EGF, and the strike-slip aftershock and its January 10 EGF. All waveforms are cut 2 seconds before the SH-wave and 4 seconds after on the transverse component. In each comparison, the red waveforms are the EGF and the black waveforms are the main event.

[*Mueller*, 1985]. The resulting STF is low-pass filtered using the corner frequency of the EGF. Similar source-time results are found when the entire waveform is deconvolved compared to when only the SH-wave is deconvolved. To resolve the STF, 60 seconds of record are used, starting a few seconds before the SH-wave to maintain high-frequency resolution. The procedure was applied to the transverse components at each station. The source-time functions from different stations were also stacked for the transverse components of the mainshock and strike-slip events to produce an average result from which to calculate the rupture duration.

The deconvolution of the third aftershock (Figure 18) from the mainshock produces an STF with a pulse-width, τ, of approximately 0.29 seconds, a time consistent with the width (0.28 seconds) of the SH pulses recorded at stations MTPU, TCRU, and SRU. The source-time functions are also consistent among the stations for the main-shock solution (Figure 18) even though some extra noise is apparent at MTPU, hence the use of the stacked functions to obtain τ.

With respect to the strike-slip event, the stacked source time function is more difficult to interpret for both the January 4 EGF and the January 10 EGF (Figure 19). When the strike-slip STFs are observed at individual stations, significant increases in the duration are visible as well as decreases in amplitude (Figure 19), suggesting that the increased durations are not solely the result of noise. Specifically, major differences in amplitude and duration are observed at stations MTPU and TCRU, suggesting rupture directivity as these stations are in opposite directions from the epicenter. MTPU and TCRU are aligned at 160° and 0° along the north-south trending plane of the

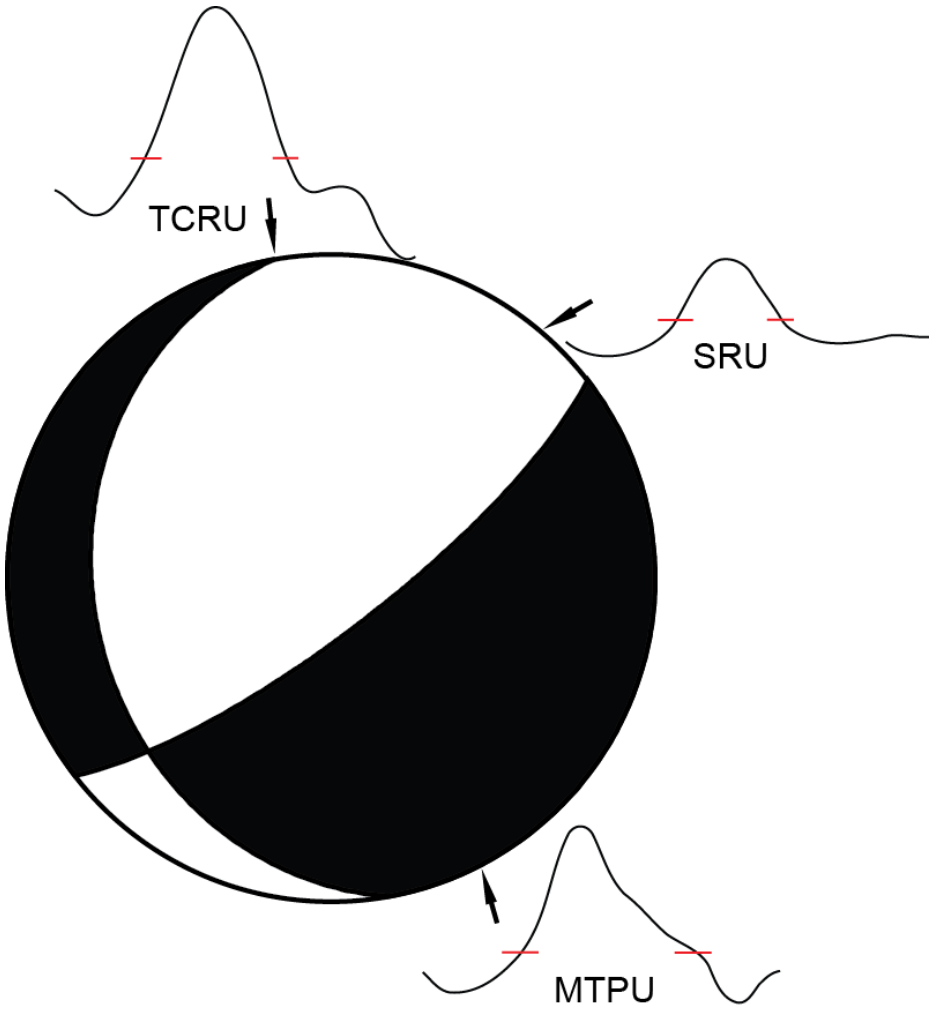

Figure 18. Mainshock source-time results. The mainshock focal mechanism is plotted with the source-time results from MTPU, SRU, and TCRU at their approximate azimuth from the event. Assuming a northward rupture on the 170° plane, MTPU has an azimuth of 160°, SRU of 70°, and TCRU of 0°. The arrows show where the STF function is related azimuthally to the earthquake. The red lines on each STF indicate the zero crossings.

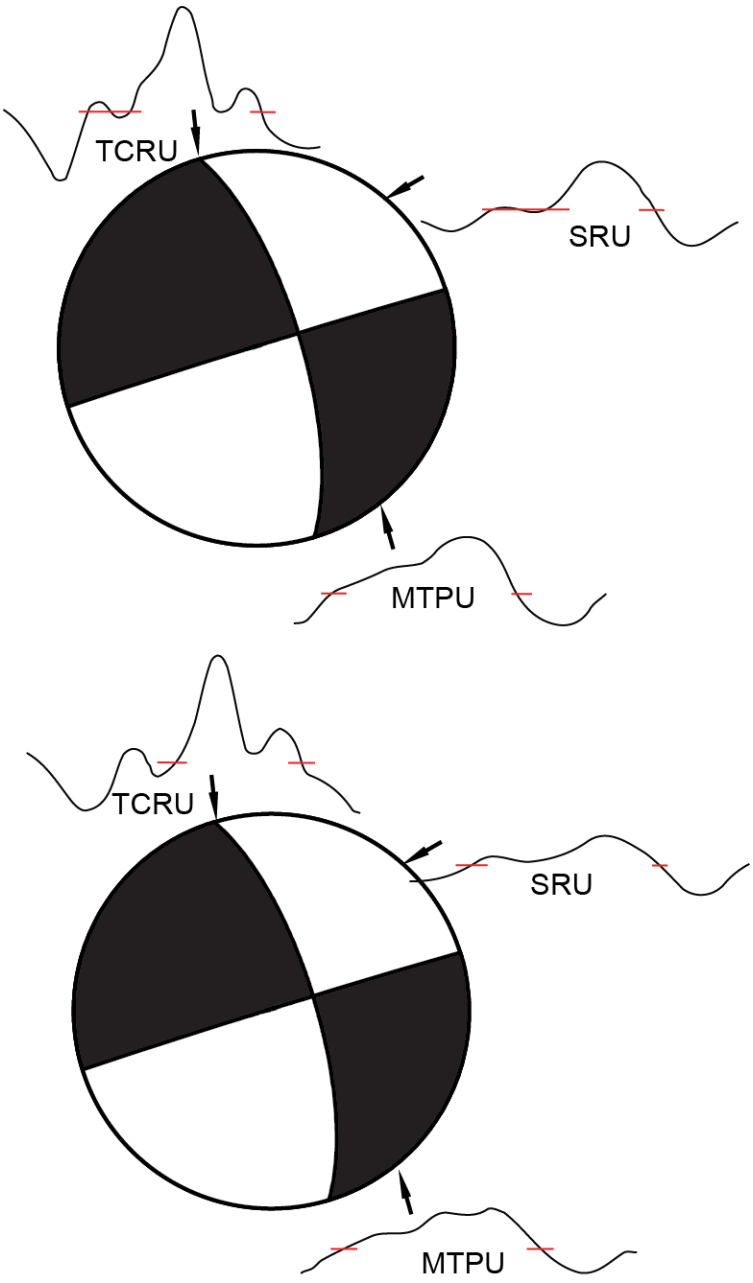

Figure 19. Strike-slip source-time results. The strike-slip focal mechanism is plotted with the source-time results for the January 4th (top) EGF and January 10th EGF (bottom) from MTPU, SRU, and TCRU at their approximate azimuth from the event (see Figure 18 for further explanation).

moment tensor focal mechanism solution for the strike-slip event, indicating a northward rupture as TCRU has a much shorter pulse width than MTPU.

4.2 Stress Drops

Earthquake rupture durations can be calculated from the source-time functions by measuring the time between zero crossings of the peak. The measured duration can then be used to calculate or estimate fault dimensions as well as quantify the stress drop. To estimate these parameters, a rupture model is assumed as different equations are used for a radial rupture versus a unilateral rupture.

For the mainshock, a circular model was chosen as the source-time function does not indicate directivity, and the distribution of aftershocks after one and three days (Figure 20) exhibit a roughly circular zone around the mainshock. *Cohn et al.* [1982] used similar aftershock distribution evidence in the 1975 Oroville California to justify using a circular model. However, the strike-slip event could not have ruptured radially given the evidence for directivity based on stations MTPU and TCRU which is more indicative of a unilateral rupture. To account for a unilateral rupture, the Haskell model was used to model the strike slip event. The Haskell model assumes a rectangular fault of length, L, the entire width, W, of which ruptures uniformly in a unilateral direction [*Haskell*, 1964].

For the mainshock, the transverse component source-time station stacks for the three results were used to obtain the rupture time, τ. For a circular model, *Cohn et al.* [1982] demonstrated that a rupture radius can be calculated from the rupture time from equation (5)

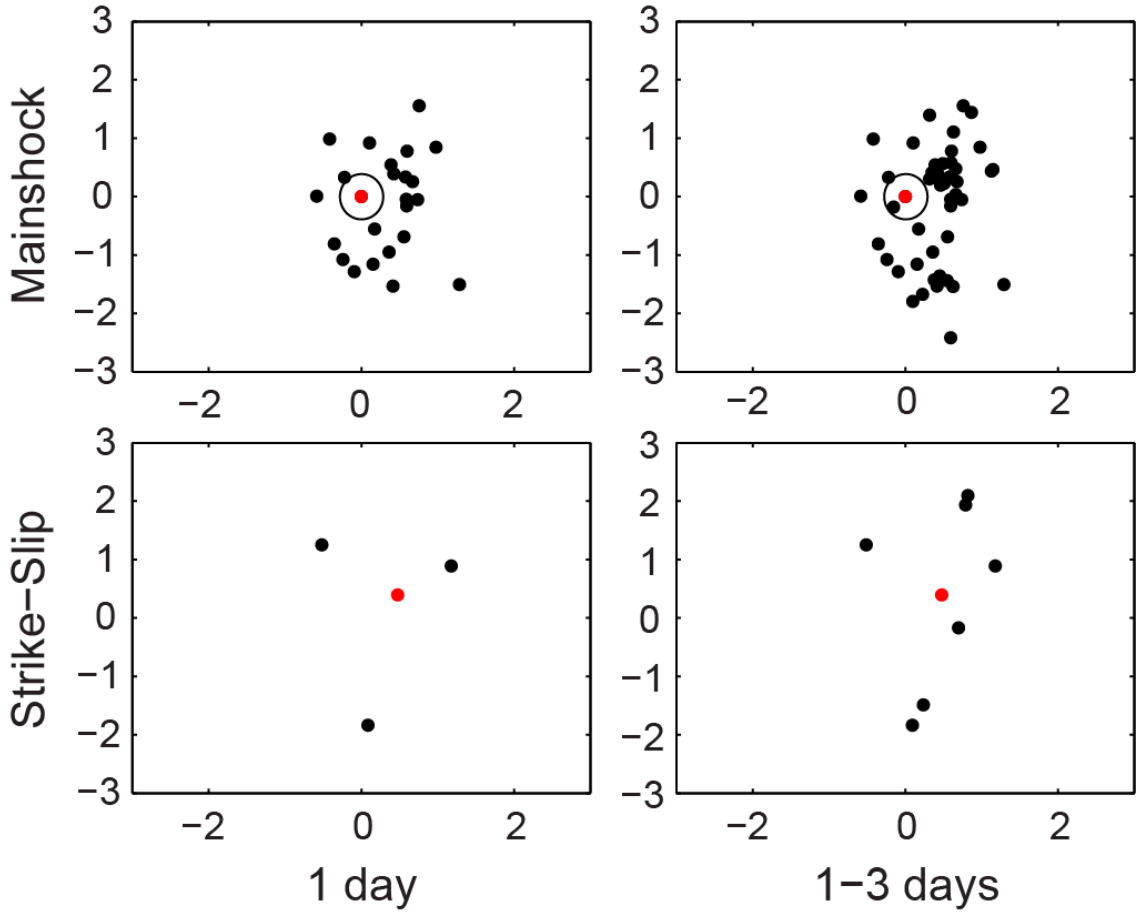

Figure 20. Mainshock and strike-slip 1-3 days aftershock plots. The first day and first 3 days of aftershocks (black dots) for the mainshock (top row, red dot) and the strike-slip aftershock (bottom row, red dot) are plotted to help determine a rupture model. The circle plotted on the mainshock plots is approximately the same radius estimated from equation (6) and indicates the potential rupture area.

$$\tau = \frac{r}{V_r} + \frac{rsin(\delta)}{\beta} + \frac{16r}{7\pi\beta} \quad (5)$$

where r is the radius, Vr is the rupture velocity, β is the S-velocity at the source depth, and sin(δ) accounts for the travel-time difference based on the fault dip angle. Estimating V_r to be 80% of β, β=3480 m/s, and sin(δ)=0.766 equation (5) simplifies to equation (6)

$$r = \frac{\tau\beta}{2.75}, \quad (6)$$

and if V_r is 50% of β, equation (5) simplifies to equation (7)

$$r = \frac{\tau\beta}{3.37}. \quad (7)$$

The stress drop for a radial rupture can then be found from the radius [*Kanamori and Anderson*, 1975] using equation (8)

$$\Delta\sigma = \frac{7M_O}{16r^3}, \quad (8)$$

where M_o is the seismic moment calculated from *Whidden and Pankow* [2012].

Entering the mainshock τ, 0.29 seconds, into equations (6) and (7) yields a rupture radius range of 290-370 meters, with rupture velocities of 50-80% of the S-velocity, β. From this range of radii and a moment of 7.1×10^{15} Nm, a minimum and maximum stress drop of 50-102 MPa was determined. This is quite large, as typical stress drops range from 1-10 MPa [*Kanamori and Brodsky*, 2004] although intraplate events have been shown to be have higher stress drops around 30 MPa [*Venkataraman and Kanamori*, 2004].

Assuming a rectangular fault model is a little more complicated as estimates must first be made for the length, L, and width, W, of the fault. However, the stress drop for a rectangular, strike-slip event can be easily calculated [*Kanamori and Anderson*, 1975] using equation (9)

$$\Delta\sigma = \frac{2}{\pi}\frac{M_O}{w^2 L}, \tag{9}$$

where M_o is the seismic moment calculated from *Whidden and Pankow* [2012]. Using the same estimate of length, the rupture duration, T_C, can be calculated using equation (10) from *Lay and Wallace* [1995]

$$T_C = \frac{L}{V_r} - \frac{L\cos\theta}{\beta}, \tag{10}$$

where L is the fault length, V_r is the rupture velocity, and β is the shear velocity at the source depth. However, T_C is not the same as τ, so the length cannot be solved for

directly; however, because these are small events with a roughly triangular STF, T_C can be compared to τ as an additional constraint.

Values for the fault length and width of the strike-slip event were estimated two different ways to first obtain upper and lower bounds on the stress drop. The upper bound was determined using the length and width values from the principal component analysis. The lower bound was estimated using a length of 400 meters, the mainshock radius, and calculating the width from the length/width ratio of 1.45, also from the principal component analysis. These estimates produced stress drops of 0.1 and 3.3 MPa, respectively. However, the predicted rupture durations, T_C, were not similar to the STF pulse-width, τ (Table 4).

Stress drop and rupture duration were calculated for L values of 600, 700, and 800 meters and the predicted T_C were compared to the observed τ (Table 4). The widths were also calculated with the PCA length/width ratio. From the comparison of the observed and predicted durations, a length of 700 meters and a corresponding width of 476 meters were determined to be the optimal fault dimensions. The predicted values of TCRU are too low to be resolved through a deconvolution procedure, but we do obtain an STF result indicating that the pulse-width is dominated by something other than the rupture duration. Predicted values for SRU were also low, but not beyond reason. MTPU, as the longest STF, is the result most dominated by the rupture duration, so the match between the predicted value and the observed value at this station was used to determine the optimal fault dimensions. The stress drop from a length of 700 meters is 0.63 MPa which is below the standard 1-10 MPa range, but the results are

Table 4. Strike-slip stress drop results.

	L (m)	W (m)	Δσ (MPa)	T_C TCRU (s)	T_C SRU (s)	T_C MTPU (s)
1	2500	1700	0.014	0.18	0.65	1.57
2	400	272	3.38	0.03	0.1	0.25
3	600	408	1	0.04	0.16	0.38
4	700	476	0.63	0.05	0.18	0.44
5	800	544	0.42	0.06	0.21	0.5
			Observed	0.2	0.28	0.4

Row 1 contains the results from the principal component analysis, row 2 contains the result using the radius for the main shock as the length, and row 3-5 are different lengths tested to determine a reasonable solution.

consistent with other estimates of stress drops of aftershocks [*Fletcher et al.*, 1984; *Hardebeck and Hauksson,* 1997].

CHAPTER 5

DISCUSSION

The combination of velocity modeling, master-event relocations, and hypoDD relocations proved highly effective in producing quality locations from which potential fault planes could be inferred. Determination of fault planes has often proved elusive in analyses of tectonic earthquakes in Utah [*Arabasz et al.*, 2007]. The final quality of locations allowed for more extensive analyses, particularly with respect to the fault-plane geometry, and the combination of the earthquake location, geometry, and source results suggests that the earthquake sequence occurred on at least two separate fault planes and that the mainshock occurred on a low-angle normal fault. Active low-angle normal faults are a topic of debate, but they have been shown to occur in the Mineral Mountains ~ 45 km to the west of the Circleville mainshock, a range that is also part of the TZ-Marysvale system [*Price*, 1998].

Supporting the theory of multiple fault planes is the distribution of normal versus strike-slip mechanisms. All of the normal-slip events for which we have solutions were located deeper than and slightly to the west of the vertical cluster of seismicity. In contrast, almost all the events known to be strike-slip were shallower than the normal events and were well-aligned with the vertical cluster. The distribution

of strike-slip events is consistent with the plane "fit" using PCA. Likewise, the distribution of normal events is consistent with the low-angle plane, a feature shared by the mainshock and January 12 aftershock.

The combination of strike-slip and normal focal mechanisms in close proximity is not an uncommon feature in the Basin and Range region or elsewhere. Paleoseismic evidence from the Sevier valley indicated both left-lateral and right-lateral strike-slip earthquakes in close proximity to normal and oblique events [*Anderson and Barnhard*, 1992]. Elsewhere in the BR, strike-slip and oblique aftershocks occurred after the 1983 Borah Peak, Idaho earthquake [*Richins et al.*, 1987] as well as the 2008 Wells, Nevada, event [*Smith et al.*, 2011], both of which were large M≥6.0 normal faulting events. The combination of strike-slip and normal events from these results could be the effect of upper-crustal motion in response to the normal event resulting in strike-slip aftershocks. The strike-slip events were shown to be shallower than the normal events, and, although some were close to the mainshock depth, this could be explained by the uncertainties in both the locations and the velocity model. This combination could also be explained by two fault planes, one normal and one strike-slip, in close proximity to each other, a combination shown to occur elsewhere in the BR as well as the Walker Lane region on the California-Nevada border [*Axen*, 1998; *Kreemer et al.*, 2009; *Lee et al.*, 2009].

The rupture characteristics of the mainshock and the strike-slip aftershock differ. The mainshock has a short rupture duration, consistent among stations, for its magnitude, producing a stress drop higher than typical values for intraplate earthquakes [*Venkataraman and Kanamori*, 2004]. Unfortunately, few stress drops have been calculated for low-angle normal fault earthquakes so it is impossible to evaluate this

result by comparing it to other studies. The only notable example is from *Abers* [1991] showing low-angle normal faults to occur off Papua New Guinea, for which he calculated rise time and moments, and from which a stress-drop could be calculated if the shear velocity at the source depth were provided. However, whereas the mainshock has a high stress drop, the strike-slip aftershock produces a low value with strong evidence of directivity. This implies significantly different rupture mechanisms. Furthermore, if the vertical fault plane is indeed different from the mainshock rupture plane, the lower stress drop and directivity are sensible results.

Lastly, while many of the results suggest both a vertical strike-slip plane and a low-angle normal fault plane, perhaps the most telling observation is the lack of evidence that the east-west, steeply dipping plane from the mainshock moment tensor solution corresponds to a fault plane. None of the events appear to fall along that plane; the first 3 days of aftershocks also do nothing to indicate the plane. While the westward protruding feature from the final locations taken as the “normal” fault plane is on the edge of resolution, the aftershock distribution within the first 1-3 days suggests that this feature is real.

CHAPTER 6

CONCLUSION

The mainshock appears to have ruptured radially along a low-angle normal fault. Whether this event occurred on a primary structure (a large or significant fault), a secondary structure (a result of local stresses), or through reactivation of an older thrust fault remains unclear, as does the maximum earthquake size that the fault can release. The mainshock rupture influenced a nearby vertical strike-slip fault which failed three days later, resulting in a large strike-slip aftershock. The activity on the strike-slip fault then perhaps in turn affected the low-angle fault, producing two more normal-slip aftershocks. The strike-slip event could also be the result of upper crustal reaction to the normal mainshock and aftershocks. The subsurface structure in the immediate region of this sequence is unclear; therefore, we cannot comment with certainty on the subsurface fault relations.

REFERENCES CITED

Abers, G. (1991), Possible seismogenic shallow-dipping normal faults in the Woodlark-D'Entrecasteaux extensional province, Papua New Guinea, *Geology*, *19*, 1205–1208.

Anderson, R. E., and T. P. Barnhard (1992), Neotectonic framework of the central Sevier Valley area, Utah, and its relationship to seismicity, in *Assesment of regional earthquake hazards and risk along the Wasatch Front, Utah: US Geological Survey Professional Paper 1500-A-J*, edited by P. L. Gori and W. W. Hays, pp. F1–F47.

Arabasz, W. J., R. Burlacu, and K. Pankow (2007), An overview of historical and contemporary seismicity in central Utah, *Central Utah Diverse Geology of a Dynamic Landscape*, *36*(4), 540.

Arabasz, W. J., and D. R. Julander (1986), Geometry of seismically active faults and crustal deformation within the Basin and Range-Colorado Plateau transition in Utah, *Extensional Tectonics of the Southwestern United States: A Perspective on Processes and Kinematics: Geological Society of America, Special Paper*, *208*, 43–74.

Arabasz, W. J., S. J. Nava, M. K. Mccarter, and K. L. Pankow (2002), *Ground-Motion Recording and Analysis of Mining-Induced Seismicity in the Trail Mountain Area , Emery County , Utah*. Technical Report, University of Utah Seismograph Stations, Salt Lake City, Utah, 168 pp.

Axen, G. (1998), The Caliente-Enterprise Zone, southeastern Nevada and southwestern Utah, *Geological Society of America Special Paper 323*, 181–194.

Cohn, S. N., T.-L. Hong, and D. V. Helmberger (1982), The Oroville Earthquakes: A study of source characteristics and site effects, *Journal of Geophysical Research*, *87*(B6), 4585, doi:10.1029/JB087iB06p04585.

Corbett, E. J. (1984), Seismicity and crustal structure studies of southern California: Tectonic implications from improved earthquake locations, 231 pp., Ph.D. Dissertation, California Institute of Technology, Pasadena, California.

Fletcher, J., J. Boatwright, L. Haar, T. Hanks, and A. R. T. Mcgarr (1984), Source Parameers for the Actershocks of the Oroville, California, Earthquake, *Bulletin of the Seismological Society of America*, *74*(4), 1101–1123.

Gomberg, J. S., K. M. Shedlock, and S. W. Roecker (1990), The effect of S-wave arrival times on the accuracy of hypocenter estimation., *Bulletin of the Seismological Society of America*, *80*(6A), 1605–1628.

Hardebeck, J. L., and E. Hauksson (1997), Static Stress Drop in the 1994 Northridge , California , Aftershock Sequence, *Bulletin of the Seismological Society of America*, *87*(6), 1495–1501.

Hardebeck, J. L., and P. M. Shearer (2002), A New Method for Determining First-Motion Focal Mechanisms, *Bulletin of the Seismological Society of America*, *92*(6), 2264–2276.

Hartzell, S. H. (1978), Earthquake aftershocks as Green's functions, *Geophysical Research Letters*, *5*(1), 1–4.

Haskell, N. A. (1964), Total energy and energy spectral density of elastic wave radiation from propagating faults, *Bulletin of the Seismological Society of America*, *54*(6A), 1811–1841.

Julander, D. R. (1983), Seismicity and correlation with fine structure in the Sevier Valley area of the Basin and Range-Colorado Plateau transition, south-central Utah, 142 pp., M.S. Thesis, University of Utah, Salt Lake City, Utah.

Kanamori, H., and D. L. Anderson (1975), Theoretical basis of some empirical relations in seismology, *Bulletin of the Seismological Society of America*, *65*(5), 1073–1095.

Kanamori, H., and E. E. Brodsky (2004), The physics of earthquakes, *Reports on Progress in Physics*, *67*(8), 1429–1496, doi:10.1088/0034-4885/67/8/R03.

Klein, F. W. (1978), *Hypocenter Location Program HYPOINVERSE*.

Kreemer, C., G. Blewitt, and W. C. Hammond (2009), Geodetic constraints on contemporary deformation in the northern Walker Lane: 2 . Velocity and strain rate tensor analysis Wa t, *The Geological Society of America Special Paper 447*, 17–31, doi:10.1130/2009.2447(02).

Lay, T., and T. C. Wallace (1995), *Modern Global Seismology*, Academic Press.

Lee, J., J. Garwood, D. F. Stockli, and J. Gosse (2009), Quaternary faulting in Queen Valley, California-Nevada: Implications for kinematics of fault-slip transfer in the eastern California shear zone-Walker Lane belt, *Geological Society of America Bulletin*, *121*(3-4), 599–614, doi:10.1130/B26352.1.

Michelini, A., and B. A. Bolt (1986), Application of the principal parameters method to the 1983 Coalinga, California, aftershock sequence, *Bulletin of the Seismological Society of America*, *76*(2), 409–420.

Mueller, C. S. (1985), Source pulse enhancement by deconvolution of an empirical Green's function, *Geophysical Research Letters*, *12*(1), 33–36.

Pechmann, J. C., W. J. Arabasz, K. L. Pankow, R. Burlacu, and M. K. McCarter (2008), Seismological Report on the 6 August 2007 Crandall Canyon Mine Collapse in Utah, *Seismological Research Letters*, *79*(5), 620–636, doi:10.1785/gssrl.79.5.620.

Price, D. E. (1998), Timing, Magnitude, and Three-Dimensional Structure of Detachment-Related Extension, Mineral Mountains, Utah, 67 pp., M.S. Thesis, University of Utah, Salt Lake City, Utah.

Richins, W., J. Pechmann, R. B. Smith, C. L. Langer, S. K. Goter, J. E. Zollweg, and J. J. King (1987), The 1983 Borah Peak, Idaho, earthquake and its aftershocks, *Bulletin of the Seismological Society of America*, *77*(3), 694–723.

Rowley, P. D. (1998), Cenozoic transverse zones and igneous belts in the Great Basin, western United States: Their tectonic and economic implications., *Geological Society of America Special Papers 323*, 195–228.

Shearer, P. M., and J. L. Hardebeck (2003), Analysis of similar event clusters in aftershocks of the 1994 Northridge, California, earthquake, *Journal of Geophysical Research*, *108*(B1), 2035, doi:10.1029/2001JB000685.

Smith, K., J. Pechmann, M. Meremonte, and K. Pankow (2011), Preliminary Analysis of the Mw 6.0 Wells , Nevada , Earthquake Sequence, *Nevada Bureau of Mines and Geology Special Publication 36*, 127–146.

Smith, R. B., and W. J. Arabasz (1991), Seismicity of the Intermountain Seismic Belt, *Neotectonics of North America*, (1), 185–228.

Standlee, L. A. (1982), Structure and stratigraphy of Jurassic rocks in central Utah: Their influence on tectonic development of the Cordilleran foreland thrust belt, in *Geological studies of the Cordilleran thrust belt*, vol. 1:Denver R, edited by R. B. Powers, pp. 357–382, Denver, Rocky Mountain Association of Geologists.

Stein, S., and M. Wysession (2003), *An Introduction to Seismology, Earthquakes, and Earth Structure*, Blackwell Publishing Ltd.

Venkataraman, A., and H. Kanamori (2004), Observational constraints on the fracture energy of subduction zone earthquakes, *Journal of Geophysical Research: Solid Earth (1978–2012)*, *109*(B5).

Waldhauser, F., and W. L. Ellsworth (2000), A Double-Difference Earthquake Location Algorithm : Method and Application to the Northern Hayward Fault , California, *Bulletin of the Seismological Society of America*, 90(6), 1353–1368.

Wannamaker, P. J. et al. (2001), Great Basin-Colorado Plateau Transition in Central Utah : An Interface Between Active Extension and Stable Interior, *Utah Geological Association Publication 30*, 1–38.

Whidden, K. M., and K. L. Pankow (2012), A Catalog of Regional Moment Tensors in Utah from 1998 to 2011, *Seismological Research Letters*, *83*(5), 775–783, doi:10.1785/0220120046.